# Bedrock geochemistry and alteration history of the clay-bearing Glen Torridon region of Gale crater, Mars

Erwin Dehouck, Agnès Cousin, Nicolas Mangold, Jens Frydenvang, Olivier Gasnault, Olivier Forni, William Rapin, Patrick J Gasda, Gwénaël Caravaca, Gaël David, et al.

# Bedrock geochemistry and alteration history of the clay-bearing Glen Torridon region of Gale crater, Mars

**Erwin Dehouck[1], Agnès Cousin[2], Nicolas Mangold[3], Jens Frydenvang[4], Olivier Gasnault[2], Olivier Forni[2], William Rapin[2], Patrick J. Gasda[5], Gwénaël Caravaca[2,3], Gaël David[2], Candice C. Bedford[6,7], Jérémie Lasue[2], Pierre-Yves Meslin[2], Kristin Rammelkamp[2], Marine Desjardins[2,8], Stéphane Le Mouélic[3], Michael T. Thorpe[9], Valerie K. Fox[10], Kristen A. Bennett[11], Alexander B. Bryk[12], Nina L. Lanza[5], Sylvestre Maurice[2], Roger C. Wiens[5]**

[1]Univ Lyon, UCBL, ENSL, UJM, CNRS, LGL-TPE, F-69622, Villeurbanne, France

[2] Institut de Recherche en Astrophysique et Planétologie, Université de Toulouse, CNRS, UPS, CNES, Observatoire Midi-Pyrénées, Toulouse, France

[3]LPG, CNRS, Université Nantes, Université Angers, Nantes, France

[4]Globe Institute, University of Copenhagen, Copenhagen, Denmark

[5]Los Alamos National Laboratory, Los Alamos, NM 87545, USA

[6]Lunar and Planetary Institute, Universities Space Research Association, Houston, Texas, USA

[7]Astromaterials Research and Exploration Science, NASA Johnson Space Center, Houston, Texas, USA

[8]UniLaSalle Beauvais, 60026 Beauvais Cedex, France

[9]Texas State University, JETS, at NASA Johnson Space Center, Houston, TX 77058, USA

[10]Department of Earth and Environmental Sciences, University of Minnesota - Twin Cities, Minneapolis, Minnesota, 55455, USA

[11]U.S. Geological Survey, Astrogeology Science Center, 2255 N Gemini Dr, Flagstaff, AZ 86001, USA

[12]Department of Earth and Planetary Science, University of California Berkeley, Berkeley, CA 94720, USA

Corresponding author: Erwin Dehouck (erwin.dehouck@univ-lyon1.fr)

**Key Points:**

- The *Curiosity* rover explored Glen Torridon, a section of Aeolis Mons previously referred to as the "clay-bearing unit" of Gale crater
- Bedrock compositions measured by ChemCam show variations correlated with changes in outcrop expression and with diagenetic overprint
- The relatively strong clay mineral signatures detected from orbit over Glen Torridon are not caused by a greater intensity of alteration

This article has been accepted for publication and undergone full peer review but has not been through the copyediting, typesetting, pagination and proofreading process, which may lead to differences between this version and the Version of Record. Please cite this article as doi: 10.1029/2021JE007103.

## Abstract

Glen Torridon is a topographic trough located on the slope of Aeolis Mons, Gale crater, Mars. It corresponds to what was previously referred to as the "clay-bearing unit", due to the relatively strong spectral signatures of clay minerals (mainly ferric smectites) detected from orbit. Starting in January 2019, the *Curiosity* rover explored Glen Torridon for more than 700 sols (Martian days). The objectives of this campaign included acquiring a detailed understanding of the geologic context in which the clay minerals were formed, and determining the intensity of aqueous alteration experienced by the sediments. Here, we present the major-element geochemistry of the bedrock as analyzed by the ChemCam instrument. Our results reveal that the two main types of bedrock exposures identified in the lower part of Glen Torridon are associated with distinct chemical compositions (K-rich and Mg-rich), for which we are able to propose mineralogical interpretations. Moreover, the topmost stratigraphic member exposed in the region displays a stronger diagenetic overprint, especially at two locations close to the unconformable contact with the overlying Stimson formation, where the bedrock composition significantly deviates from the rest of Glen Torridon. Overall, the values of the Chemical Index of Alteration determined with ChemCam are elevated by Martian standards, suggesting the formation of clay minerals through open-system weathering. However, there is no indication that the alteration was stronger than in some terrains previously visited by *Curiosity*, which in turn implies that the enhanced orbital signatures are mostly controlled by non-compositional factors.



## Plain Language Summary

In early 2019, the *Curiosity* rover embarked on a multi-year exploration of the Glen Torridon region, a topographic trough on the flank of Aeolis Mons, the sedimentary mound inside Gale crater, Mars. Orbital instruments have detected clay minerals over Glen Torridon, making it a primary target for *Curiosity*, because clay minerals are indicators of past interactions with water, and provide a medium favorable to the preservation of organic compounds. Understanding the context of formation of the clay minerals, and determining how much the sediments have been altered by water were among the objectives of the Glen Torridon campaign. Based on the chemical compositions measured by the ChemCam instrument, we show that the amount of water that interacted with the sediments was high enough to take away part of the most soluble elements. Nonetheless, similar levels of alteration have been observed in other parts of Gale, which implies that the signal observed from orbit is not controlled solely by the abundance of clay minerals in the rocks. Finally, in the highest part of Glen Torridon, we analyzed an area of light-toned rocks with distinct chemical compositions, which likely result from further modification by groundwater long after the main phase of alteration.


## 1 Introduction

Since its landing on Mars in August 2012, the Mars Science Laboratory (MSL) rover *Curiosity* has been continuously investigating the sedimentary rock record of Gale crater in search of past habitable environments (Grotzinger et al., 2012). During the first two years of the mission, the rover studied the fluvio-deltaic and lacustrine deposits of Aeolis Palus (Grotzinger et al., 2014, 2015), after which it reached the foothills of Aeolis Mons (or, informally, Mt. Sharp), the central mound of Gale crater. From there, it steadily gained elevation and explored more than 300 meters of stratigraphy, mostly within the mudstone-dominated Murray formation (e.g., Mangold et al., 2019; Stein et al., 2018). In January of 2019, after completing its exploration of Vera Rubin ridge (VRR), an erosion-resistant section of the Murray formation (Fraeman et al., 2020), *Curiosity* entered a new region informally

named Glen Torridon (GT), corresponding to the shallow "valley" immediately south of VRR (Fox et al., 2020; Bennett et al., this issue) (Figure 1).

The Glen Torridon region has been a primary target of the mission ever since the successful landing, because it displays the clearest orbital signatures of clay minerals in the part of Gale crater explored by *Curiosity* (Grotzinger et al., 2012; Milliken et al., 2010). Specifically, the importance of this region in the context of MSL science objectives is twofold. First, clay minerals are known to enhance the preservation of organic matter in the sedimentary record (Summons et al., 2011), thus making Glen Torridon a region of particular interest for the potential detection of ancient biosignatures. Second, the "clay-bearing unit" of Gale crater—as Glen Torridon was previously referred to—is overlaid by a younger "sulfate-bearing unit" (Fraeman et al., 2016; Milliken et al., 2010), and this stratigraphic relationship is thought to be representative of the "clay-to-sulfate" mineralogical transition observed at a global scale (Bibring et al., 2006; Carter et al., 2013), which in turn could be the mark of a major climate change that occurred around the Late Noachian–Early Hesperian boundary. For these reasons, the *in situ* characterization of the clay-bearing rocks of Glen Torridon, as well as their detailed geologic and geochemical settings, may provide crucial insights into how the habitability and environmental conditions of early Mars have evolved over time.

Another interest of the Glen Torridon region lies in the comparison of *in situ* and orbital observations. X-ray diffraction (XRD) analyses performed by the CheMin instrument (Blake et al., 2012) have revealed the presence of clay minerals in significant abundances (up to ~30 wt%) at several locations along *Curiosity*'s traverse leading up to Glen Torridon where orbital detections of such clay minerals were tenuous or absent (Bristow et al., 2018; Rampe et al., 2017; Vaniman et al., 2014). Thus, one objective of the MSL team for the Glen Torridon campaign was to better understand why the orbital signatures of clay minerals are more spatially extensive in this region compared to previous terrains, and, specifically, to determine if they are explained by a higher abundance of clay minerals (and thus by more intense alteration in the past), or by extrinsic factors such as dust/sand cover or outcrop expression (Fox et al., 2020; Bennett et al., this issue).

In this contribution, we report the findings of the ChemCam instrument throughout Glen Torridon, with a focus on the major-element geochemistry of the bedrock. In section 2, we describe how our data were acquired, processed and classified. In section 3, we present the results in four subsections corresponding to the main subregions visited by *Curiosity* along her traverse: the Jura member (Jm) of the Murray formation, the Knockfarril Hill member (KHm) of the Carolyn Shoemaker formation, the Buttes, and finally the eastward traverse within the Glasgow member (Gm) of the Carolyn Shoemaker formation (Figure 1). The Buttes encompass both the Knockfarril Hill and Glasgow members (Figure 1; Bennett et al., this issue), but are treated separately owing to their compositional uniqueness. In section 4, we compare our results with the mineralogy of the drill samples analyzed by the CheMin XRD instrument, and discuss on this basis the alteration history of the region; finally, we also discuss the implications of our findings for the orbital observations of Gale crater.

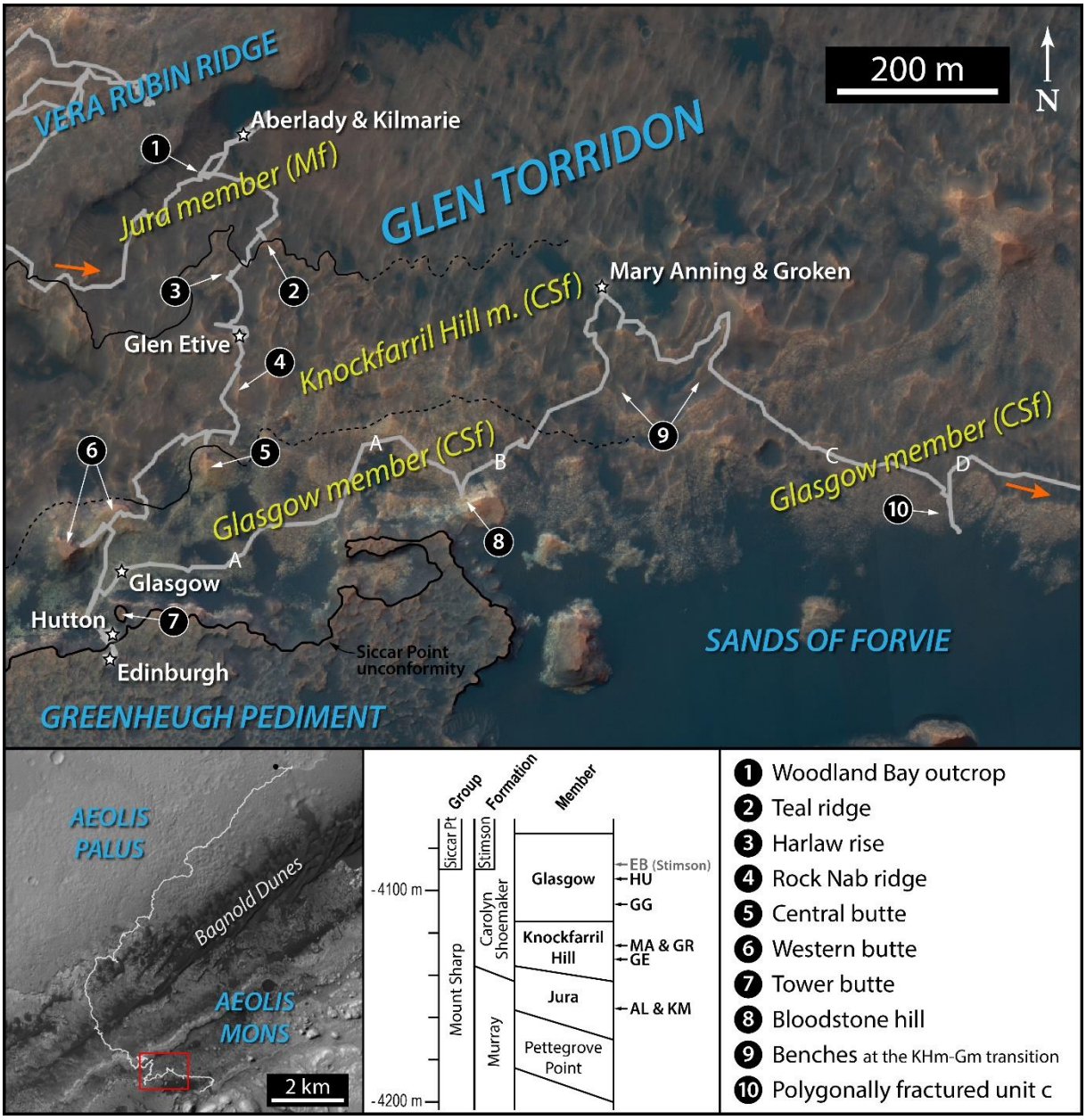


**Figure 1.** Context map of *Curiosity*'s traverse through Glen Torridon (white line), highlighting the three stratigraphic members identified in the region. As shown by the stratigraphic column (lower center panel), the Jura member is the topmost member of the Murray formation, whereas the Knockfarril Hill and Glasgow members are the two lowermost members of the Carolyn Shoemaker formation (see Figure S1 for the full stratigraphic column). On the map, member boundaries are drawn as solid black lines where they are known with confidence, and as dashed lines where their location is less certain. At the time of writing, member boundaries have not been mapped in the eastern part of the region. The thicker line represents the unconformity between the Mount Sharp and Siccar Point groups. The two orange arrows show the direction of *Curiosity*'s movement, as well as the approximate start and end points of the campaign described in this paper. White stars indicate drill site locations (the Edinburgh drill site, which samples the Stimson formation, is shown for context but is not included in this study). The drill sites are also located on the stratigraphic column (AL = Aberlady; KM = Kilmarie; GE = Glen Etive; MA = Mary Anning; GR = Groken; GG = Glasgow; HU = Hutton; EB = Edinburgh). Other locations visited by

*Curiosity* are numbered from 1 to 10 (key in lower right panel). "Polygonally fractured unit c" is from Hughes (2021). The letters A, B, C and D correspond to the four sections of the lateral traverse within the Glasgow member (see section 3.4). The lower left panel shows the location of Glen Torridon at the scale of the entire traverse, as of mid-June 2021.

## 2 Data and methods

### 2.1 Data acquisition and processing

The main scientific task of the ChemCam instrument is to measure the chemical composition of rock and soil targets within a few meters of *Curiosity* using Laser-Induced Breakdown Spectroscopy (LIBS) (Maurice et al., 2012; Wiens et al., 2012). Each ChemCam LIBS analysis of a given target consists of a raster of several points (usually between 5 and 20) from about one half to a few millimeters apart from each other. Each LIBS point samples a surface of ~350-550 µm in diameter (depending on the distance of the target to the instrument) and a depth of a few tens to hundreds of microns through a series of laser shots—typically 30, but up to several hundreds when performing a "depth profile" activity (Maurice et al., 2012, 2016; Wiens et al., 2012). The light emitted by the laser-induced plasma is collected for each shot and its spectrum is recorded; following spectral processing, this is referred to as a LIBS spectrum (Wiens et al., 2013). Because eolian dust is ubiquitous on Mars, including at Gale crater (e.g., Lasue et al., 2018; Schmidt et al., 2018), the spectra corresponding to the first five shots of a given point are set aside; the remaining spectra are averaged, and it is this average spectrum that is typically processed to determine the chemical composition. "Shot-to-shot" investigations—i.e., using spectra from individual laser shots instead of the average spectrum—can also be of interest to search for mineral endmembers, for example.

Quantification of eight major rock-forming oxides—$SiO_2$, $TiO_2$, $Al_2O_3$, $FeO_T$, MgO, CaO, $Na_2O$ and $K_2O$—is performed routinely, and the result is referred to as the MOC (for "major-element oxide composition"). Briefly, the MOC is the weighted average of two multivariate calibration models, the "partial least squares 1" (PLS1) and the "independent component analysis" (ICA), which were both developed using the same set of 408 geochemical standards analyzed with the ChemCam replica of the Los Alamos National Laboratory, under Mars-like conditions (Clegg et al., 2017). A ninth oxide, MnO, was recently added to the MOC following the development of a dedicated calibration model (Gasda et al., 2021). The accuracy of the MOC is estimated by calculating the root mean squared error of prediction (RMSEP) for a representative test set of the calibration database (Clegg et al., 2017). The accuracy varies with actual composition, therefore it is reported for each ChemCam measurement (Table S1). However, to facilitate graphical representations, we calculated the average accuracy of each oxide for the Glen Torridon bedrock (Table S2). The precision, on the other hand, is estimated using the standard deviation of multiple observations of homogenous targets and has been shown to be better than the accuracy (Blaney et al., 2014; Mangold et al., 2015). Because this work focuses on compositional variations, the precision is the most relevant indicator of the relative error between the measurements; it is reported in Table S2.

In addition to the major oxides listed above, the presence and abundance of a number of other elements—including H, Li, B, F, P, S, Cl, Cr, Ni, Cu, Zn, Rb, Sr and Ba—can also be investigated with ChemCam data (Forni et al., 2015; Gasda et al., 2017; Lasue et al., 2016; Nachon et al., 2017; Payré et al., 2017, 2019; Rapin et al., 2019; Schröder et al., 2015; Wiens et al., 2013; Goetz et al., this issue). Although we focus here on the MOC results, we also

make use of volatile/minor elements whenever appropriate to better understand the mineralogy and geologic processes that may explain the chemical variations observed.

In this study, we use all LIBS targets from Glen Torridon that were located less than 6 meters from the instrument. Only 4 targets were located farther away, 3 of which were iron meteorites. For targets located beyond 3.5 m (which represent less than 5% of our dataset), we applied the empirical distance correction proposed by Wiens et al. (2021), which improves the MOC quantification model for $SiO_2$, $Al_2O_3$, $Na_2O$ and $K_2O$ at long distances.

In addition to LIBS spectra, ChemCam also acquires high-resolution images of each target using its Remote Micro-Imager (RMI) (Le Mouélic et al., 2015; Maurice et al., 2012). Combined with information on the movements of the rover mast, these images allow the precise localization and geologic contextualization of the LIBS points.

### 2.2 Data selection and classification

Between sols 2301 and 3007 (a "sol" is a Martian solar day, and sol 0 is the day of *Curiosity*'s landing on Mars), ChemCam analyzed a total of 818 targets in Glen Torridon and on the Greenheugh pediment, corresponding to 7349 LIBS analysis points. To extract meaningful compositional information from this large dataset, it was necessary to carefully classify each analysis point. First, those having suboptimal or uncertain focus were flagged. The quality of the focus is checked using a "focus curve" quantifying the RMI sharpness as a function of focal distance (Peret et al., 2016); such a curve is returned by the instrument each time an autofocus is performed (typically 2-4 times per LIBS raster). For example, if the maximum of the curve is at the edge of the range of distances scanned by the autofocus, it is likely that the best focus position was missed. Poor focus often results in lower signal intensity in the LIBS data, relative to other points of the raster, which provides an additional criterion for identifying points that are not optimally focused between autofocuses. Second, each point was associated with a type of material—such as "bedrock", "diagenetic feature", "float rock" or "soil"—based on visual evaluation of Navcam (Navigation cameras; Maki et al., 2012), Mastcam (Mast cameras; Malin et al., 2017) and RMI images. Subtypes were also added when deemed useful, in particular to distinguish the various morphologies and textures of the bedrock (e.g., "rubbly", "coherent", etc.). Points that appeared to have sampled more than one type of material (e.g., bedrock with soil cover, edge of a vein, etc.) or that hit shadowed areas were classified as "mixture/unclear" and generally not used. Third, details related to the geographic (e.g., "Teal ridge") and stratigraphic localization (e.g., "Knockfarril Hill member") of the target were also assigned to each analysis point. The full classification is provided in Table S1.

As shown by previous studies (Frydenvang et al., 2020; Mangold et al., 2015, 2019), this point-by-point approach is critical for the accurate characterization of the geochemistry of the bedrock, because the presence of diagenetic features (especially Ca-sulfate veins, which are widespread at Gale crater; e.g., Kronyak et al., 2019; L'Haridon et al., 2018, 2020; Nachon et al., 2014, 2017; Rapin et al., 2016) or soil cover could bias the measured composition if all points were averaged blindly.

### 2.3 Chemical Index of Alteration

In addition to variations in oxide or element abundances, we also tracked throughout the rover traverse the value of the Chemical Index of Alteration (CIA), which is calculated using the following formula (Nesbitt & Young, 1982):

$$\mathrm{CIA} = \frac{\mathrm{Al_2O_3}}{\mathrm{Al_2O_3} + \mathrm{CaO^*} + \mathrm{Na_2O} + \mathrm{K_2O}} \times 100$$

with oxide abundances expressed in moles. The asterisk (*) indicates that only CaO from the silicate fraction of the rock should be included in the calculation (Nesbitt & Young, 1982). Therefore, any Ca-sulfate material contributing to the composition measured by ChemCam would tend to an overestimation of CaO*, and thus to an underestimation of the CIA. To mitigate this issue, we only included in our CIA calculations the LIBS points associated with the "bedrock" type in our classification (i.e., we excluded other types such as "diagenetic feature" or "mixture/unclear"). However, this selection can miss some Ca-sulfate contributions, because small veins or cements are not always visible on the RMI images (e.g., Gasda et al., this issue). To further minimize such contributions in bedrock targets from the Murray and Carolyn Shoemaker formations, we filtered out the LIBS points having both a sum of oxides <95 wt% (the presence of sulfates decreases the sum of oxides because $SO_3$ is not currently included in the MOC; Clegg et al., 2017) and a CaO abundance >5 wt% (i.e., ~2.5 times higher than the median CaO value of the Glen Torridon bedrock). The points removed by this method represent ~5% of the total number of bedrock points. They define a clear trend toward the Ca-sulfate endmember, which confirms that the filter works as intended and thus minimizes the detrimental effect on the calculated CIA values (see details in Text S1).

## 3. Results

In this section, we present the geochemical variations observed by ChemCam along the rover traverse throughout Glen Torridon. Each subsection corresponds to a subregion, following the main stratigraphic divisions identified by the MSL team (Figure 1); however, the data from Central butte, Western butte and Tower butte (Figure 1)—collectively referred to as "the Buttes" in this paper—are treated separately owing to their geochemical uniqueness. We focus here on the composition of the bedrock; the analyses of diagenetic features by ChemCam are described in more detail in Gasda et al. (this issue).

### 3.1 Jura member

The rover departed Vera Rubin ridge and entered Glen Torridon on sol 2302, i.e., January 26$^{th}$, 2019 (Fraeman et al., 2020). Due to the topography of the ridge, it initially went down in elevation (from -4140 m on sol 2300 to -4158 m on sol 2413), and thus remained in the Jura member first identified on VRR (Figures 1 and S1) (Edgar et al., 2020). In this paper, unless otherwise noted, the term "Jura member" (Jm) will refer solely to the part of the member exposed within Glen Torridon.

The transition between the two regions is marked by a noticeable change in outcrop expression (Figure S2), with the appearance of the "rubbly bedrock", so called because it is mainly composed of small blocks embedded in soil material (Figure 2c). These blocks are very fine-grained (mostly mudstones; Caravaca et al., this issue) and the uniformity of their composition (see below) indicates that they are mostly in-place, hence their classification as bedrock. In addition, a second bedrock type composed of larger and coarser-grained slabs (displaying cm-scale cross-stratifications in some places; Caravaca et al., this issue) was identified in a few locations on the floor of the Jura member, and is referred to as the "coherent bedrock" (Figure 2c).

The ChemCam analyses performed on the two types of bedrock reveal that they differ not only in their outcrop expression and texture, but also in their chemical composition (Figure 2a-b and Table 1). The slabs of coherent bedrock are primarily characterized by an enrichment in MgO (most points are >6 wt%) compared to the rubbly bedrock. Conversely, the rubbly bedrock is mainly characterized by an enrichment in both $K_2O$ (>1.5 wt%) and $SiO_2$ (>55 wt%) compared to the coherent bedrock; it is also slightly enriched in $FeO_T$ and

depleted in CaO (Table 1). When taken together, the two types of bedrock span the full range of variability observed previously in the Murray formation for MgO, $K_2O$ and $SiO_2$ (Frydenvang et al., 2020). Moreover, most of the smaller rocks (granules, pebbles and cobbles in terms of grain size) found on the floor of the Jura member show compositions in line with the rubbly bedrock (Figure 2a-b), which indicates that they are displaced and/or more degraded pieces of it. However, a few rounded pebbles have a composition similar to the coherent bedrock (target Gardenstown, sol 2349). The fine-grained soils have a composition in line with previous soils and sand dunes analyzed by ChemCam at Gale crater (Cousin et al., 2017a), which suggests that any contribution to the soil fraction from the local rocks is insignificant.

It is important to emphasize that the number of data points for the two types of bedrock reported in Table 1 does not reflect their respective areal exposure in the field. As illustrated in Figure 2c, the rubbly bedrock dominates the landscape and is in fact responsible for the smooth appearance of the northern Glen Torridon region in orbital imagery (Figure 1). As a consequence, most of the rover traverse in the Jura member occurred over rubbly bedrock and pebble-strewn areas, and it is because the stops were chosen to occur near more coherent outcrops that there is a relatively high number of data points on this less abundant type of bedrock. Moreover, being composed of small blocks, the rubbly bedrock was not favorable for drilling; therefore, the two drill samples of the Jura member (named Aberlady and Kilmarie) analyzed by the CheMin and SAM (Sample Analysis at Mars; Mahaffy et al., 2012) instruments were taken from slabs of coherent bedrock (Figure 2c).

In addition to the coherent and rubbly, a third type of bedrock was observed in the Jura member, at the Woodland Bay outcrop (location #1 in Figure 1). This outcrop displays a specific pattern of alternating massive/more resistant and laminated/more recessive layers (Figure 3c; see also Caravaca et al., this issue). This pattern has been referred to as the "Flodigarry facies" (after the eponymous target from sol 2356) in some previous studies, and interpreted as the base of the Jura member (Bristow et al., 2021; Edgar et al., 2020; Fedo et al., 2020). The Woodland Bay outcrop also displays some layers with a distinctive pattern of polygonal fractures (Figure 3c; see also Caravaca et al., this issue), which were observed at several locations across the Jura member and were hypothesized to be the source of the abundant pebbles in the area.

Geochemically, the targets of the Woodland Bay outcrop overlap with the rest of the Jura bedrock (Figure 3a-b). The recessive layers are the closest match to the coherent endmember, having elevated MgO and low $K_2O$ and $SiO_2$, whereas the resistant layers have a more intermediate composition between the coherent and rubbly endmembers. Finally, the polygonally fractured layers tend to have elevated $K_2O$ and $SiO_2$, but their MgO content does not match the rubbly endmember, making them unlikely to be a significant source of pebbles as hypothesized when they were first observed.

Overall, the GT Jura bedrock (all types included) is characterized by a strong negative correlation between MgO and $K_2O$ (Pearson coefficient: -0.82; Table S3), and an almost equally strong positive correlation between $SiO_2$ and $K_2O$ (+0.81). There are also notable positive correlations between $Al_2O_3$ and $Na_2O$ (+0.64), and between MgO and CaO (+0.51). The average CIA values are elevated (~57-58) for the three bedrock types (Table 1).

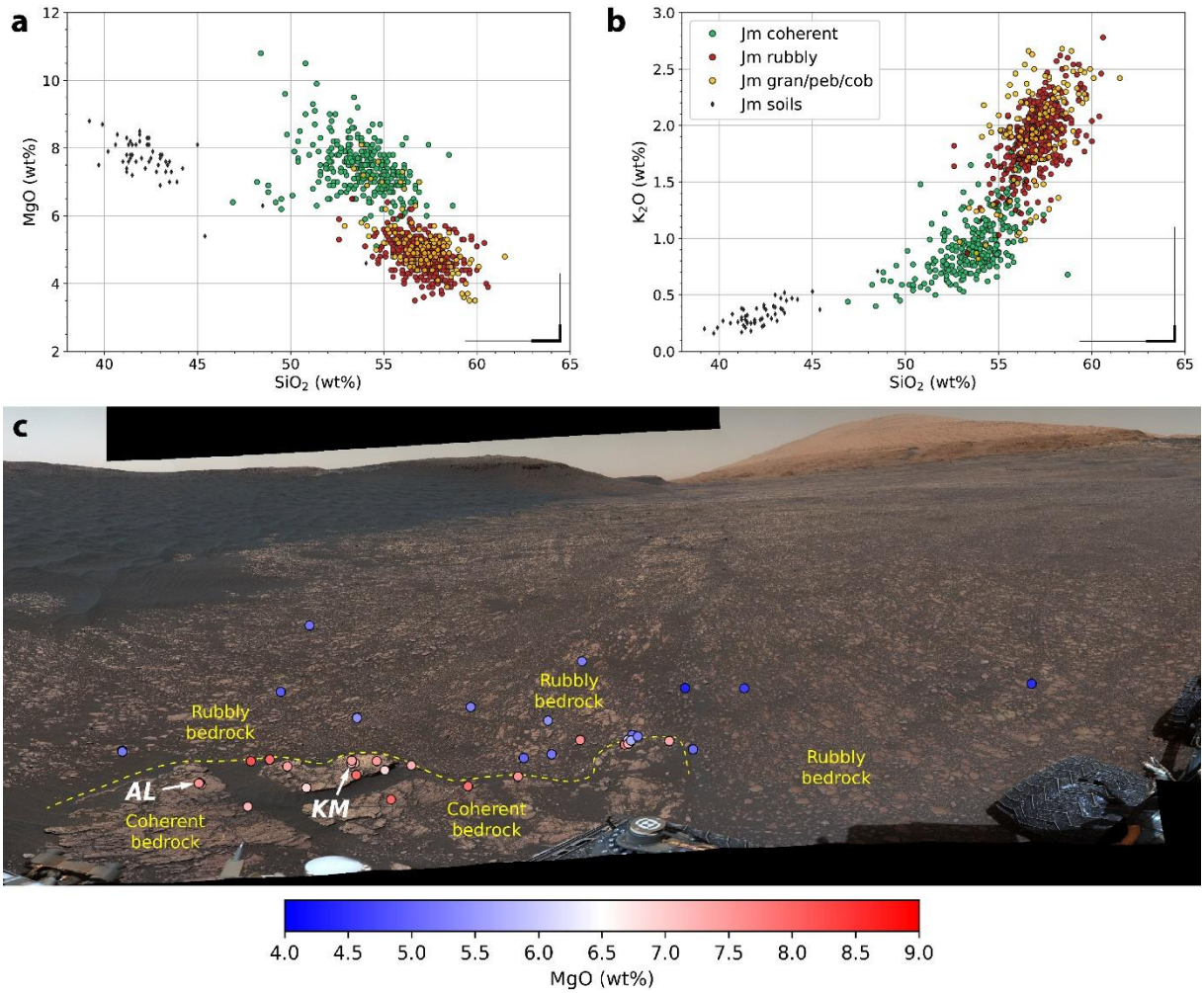


**Figure 2.** Major-element oxide composition of the coherent bedrock, rubbly bedrock, granules/pebbles/cobbles ("gran/peb/cob" in the legend) and soils in the Jura member. (a, b) MgO vs $SiO_2$ and $K_2O$ vs $SiO_2$ plots. Each symbol corresponds to a single LIBS point and is color-coded according to the type of target (see legend in panel b). The error bars in the lower right corner of each plot represent the accuracy (thin line) and precision (thick line) of the relevant oxides. The distinction between coherent and rubbly targets is based on visual evaluation alone (see section 2.2). (c) Compositional map around the Aberlady (AL) and Kilmarie (KM) drill holes (see localization in Figure 1), showing the average MgO content of ChemCam targets projected on a Mastcam color mosaic (mcam12601, sol 2375; credits: NASA/JPL-Caltech/MSSS). The dashed line represents the approximate boundary between the coherent and rubbly bedrock, inferred from imagery and chemistry. For scale in the foreground, the rover wheels measure 40 cm in width, and the AL and KM drill holes are about 80 cm away from each other. The Vera Rubin ridge and Mt Sharp are visible in the background, to the left and right, respectively.

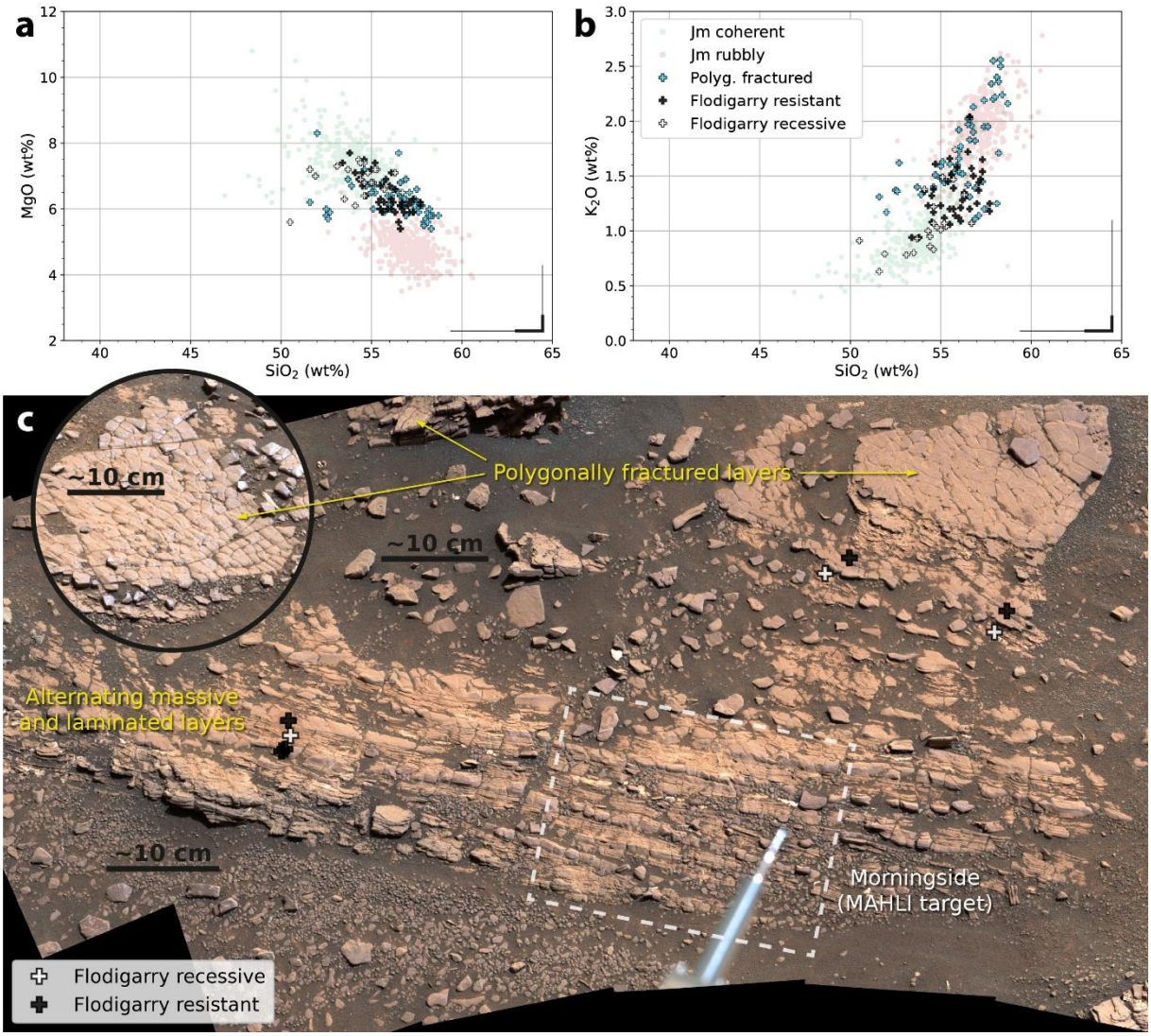


**Figure 3.** Major-element oxide composition of the recessive, resistant and polygonally fractured layers of the Woodland Bay outcrop, Jura member. (a, b) MgO vs $SiO_2$ and $K_2O$ vs $SiO_2$ plots. The error bars in the lower right corner of each plot represent the accuracy (thin line) and precision (thick line) of the relevant oxides. Each symbol corresponds to a single LIBS point and is color-coded according to the type of target (see legend in panel b). Jura coherent and rubbly bedrock compositions are taken from Figure 2 and displayed as semi-transparent points to show where the Woodland Bay outcrop compositions plot comparatively. Note that the polygonally fractured category includes targets with a similar pattern observed elsewhere in the Jura member. (c) Mastcam color mosaic (mcam12854, sol 2427; credits: NASA/JPL-Caltech/MSSS) of the Woodland Bay outcrop, showing the ChemCam targets that analyzed the recessive and resistant layers. Each symbol corresponds to the center of a LIBS raster of 5 or 10 points. The white rectangle shows the approximate location of the MAHLI (Mars Hand Lens Imager, Edgett et al., 2012) target Morningside, described in detail in Caravaca et al. (this issue). ChemCam targets that analyzed the polygonally fractured material are not visible in this mosaic, but examples of this texture are highlighted. The inset shows another portion of the outcrop located ~80 cm to the right of the main image, where the polygonal pattern is particularly well expressed (mcam12841, sol 2424; credits: NASA/JPL-Caltech/MSSS).

**Table 1.** *Average chemical compositions of the GT Jura bedrock measured by ChemCam, in wt%.*

| Subset | N[a] | $SiO_2$ | $TiO_2$ | $Al_2O_3$ | $FeO_T$ | MgO | CaO | $Na_2O$ | $K_2O$ | MnO | Sum | CIA |
|---|---|---|---|---|---|---|---|---|---|---|---|---|
| Coherent | 297 | 53.8 (1.8) | 1.02 (0.30) | 11.8 (1.3) | 18.1 (1.0) | 7.4 (0.8) | 2.0 (0.7) | 2.65 (0.28) | 0.99 (0.32) | 0.10 (0.12) | 97.97 (2.08) | 56.6 (3.3) |
| Rubbly | 367 | 57.1 (1.2) | 0.97 (0.07) | 11.9 (1.0) | 19.1 (0.9) | 4.8 (0.5) | 1.2 (0.3) | 2.64 (0.22) | 1.91 (0.28) | 0.03 (0.03) | 99.76 (1.78) | 58.0 (1.9) |
| Flodigarry | 184 | 55.7 (1.6) | 0.97 (0.11) | 11.5 (1.1) | 18.8 (0.9) | 6.2 (0.7) | 1.5 (0.4) | 2.45 (0.26) | 1.51 (0.38) | 0.03 (0.04) | 98.71 (2.37) | 57.9 (2.0) |

*Note.* Standard deviations (1σ) are given in parentheses. See text for details about the subsets.
[a]N = number of LIBS points used for the calculations.

3.2 Knockfarril Hill member

The Knockfarril Hill member (KHm) overlies the Jura member and marks the base of the recently defined Carolyn Shoemaker formation (Figures 1 and S1; Bennett et al., this issue). Like in the Jura member, we classified the bedrock targets within the Knockfarril Hill member into two main types based on their outcrop expression: the coherent bedrock, which forms large slabs and erosion-resistant outcrops, and the rubbly bedrock, which is composed of smaller blocks often associated with pebble-strewn areas. However, in the Knockfarril Hill member, it is the coherent bedrock that is spatially dominant (Caravaca et al., this issue), and—perhaps as a consequence of being more abundant—it also displays greater geochemical variability than its Jura counterpart. Therefore, it is necessary to treat separately the different areas visited by *Curiosity* within this member.

Like its Jura counterpart, the rubbly bedrock of the Knockfarril Hill member is characterized by elevated $K_2O$ and $SiO_2$ content, and low MgO content (Figure 4a-b). One area in particular, near the Rock Nab ridge (location #4 in Figure 1), displays an average MgO content of 4.1 wt% (Table 2), at the very low end of the values observed in the Jura member.

ChemCam obtained its first compositional measurements of the Knockfarril Hill member on sol 2440, at Teal ridge (location #2 in Figure 1), where the bedrock is classified as "coherent" and shows a chemical composition very similar to the coherent endmember of the Jura member in terms of MgO, $K_2O$ and $SiO_2$ contents (Figure 4c-d; Table 2). In contrast, the next two areas, named Harlaw rise and Glen Etive (locations #3 and #4 in Figure 1, visited between sols 2450 and 2553), show more intermediate MgO abundances (i.e., intermediate between the coherent and rubbly endmembers of the Jura member), as well as higher $K_2O$ and $SiO_2$ contents. In fact, the average $K_2O$ content of the Glen Etive bedrock (1.89 wt%) is almost equal to the one of the Jura rubbly endmember (1.91 wt%). $Na_2O$ does not follow the same trend, since it is slightly lower at Harlaw rise and Glen Etive compared to Teal ridge and the Jura coherent endmember (Tables 1 and 2).

The last area visited within the Knockfarril Hill member, named Mary Anning, is located ~450 m to the east of Glen Etive—it was visited between sols 2825 and 2921, after a lateral traverse through the Glasgow member (Figure 1). Although the bedrock composition at Mary Anning is overall in line with the areas described above (considering their variability), it stands out on several aspects. First, it displays the highest MgO abundances of the Glen Torridon region (and among the highest of the Mt Sharp group bedrock; Frydenvang et al., 2020): ~9 wt% on average, and up to ~15 wt% on individual LIBS points (Figure 4c; Table 2). Second, although the average $FeO_T$ content is slightly lower than in other Knockfarril Hill areas, a number of LIBS points that sampled a knobby-looking bedrock layer show elevated $FeO_T$ abundances (up to ~30 wt% according to the MOC model; Figure 5a-b). Conversely, these points are depleted in several other oxides, especially $SiO_2$ (down to ~37 wt%) and MgO (down to ~4 wt%), which creates the trends toward the origin in Figure 4c-d. Gasda et

al. (this issue) hypothesized that this material is either cemented by iron oxides and/or contains small Fe-rich nodules. Siderite, which has been detected in small amounts by CheMin in the Mary Anning drill samples (Thorpe et al., this issue), is another candidate, although ChemCam does not observe an enhanced carbon signal for these targets. Lastly, Mary Anning is also characterized by enrichments in MnO, particularly in discrete, dark-toned nodules located around the Groken drill hole (Gasda et al., this issue; Lanza et al., 2021), but also in the bedrock in the general area (Table 2).

Overall, the Knockfarril Hill bedrock is characterized by a negative correlation between MgO and $K_2O$ (Pearson coefficient: -0.60; Table S4), and a positive correlation between $SiO_2$ and $K_2O$ (+0.70), but both are slightly less strong than in the Jura member. $Al_2O_3$ is almost equally correlated to $Na_2O$ (+0.65) than in Jura. There is also a notable negative correlation between MgO and $FeO_T$ (-0.57). Finally, the average CIA values remain elevated (~55-57) in all the main areas visited by the rover (Table 2).

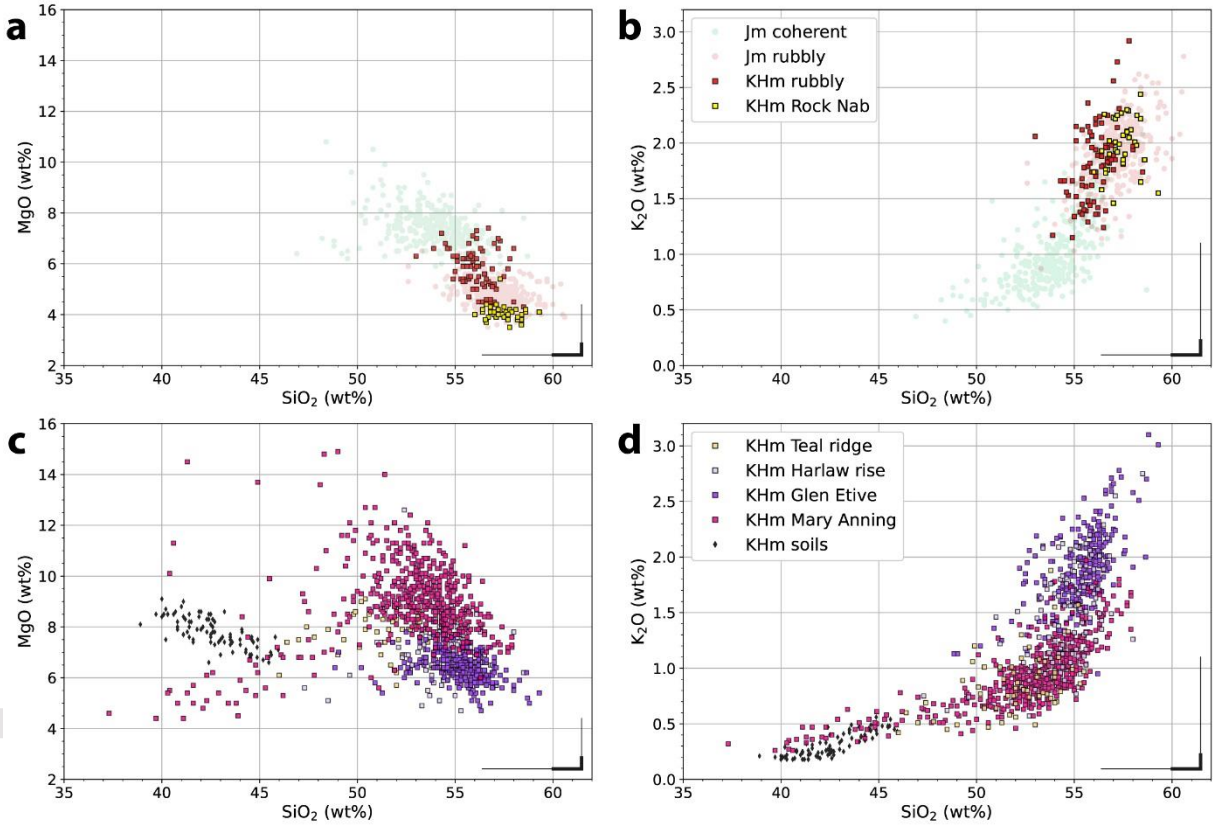


**Figure 4.** Major-element oxide compositions of the bedrock of the Knockfarril Hill member (KHm). MgO vs $SiO_2$ and $K_2O$ vs $SiO_2$ plots for the rubbly bedrock (a, b) and for the coherent bedrock (c, d). The error bars in the lower right corner of each plot represent the accuracy (thin line) and precision (thick line) of the relevant oxides. Each symbol corresponds to a single LIBS point and is color-coded according to the type of target and/or geographic location (see legends in panels b and d). In the two top panels, Jura coherent and rubbly bedrock compositions are taken from Figure 2 and displayed as semi-transparent points to show where the KHm rubbly targets plot comparatively.

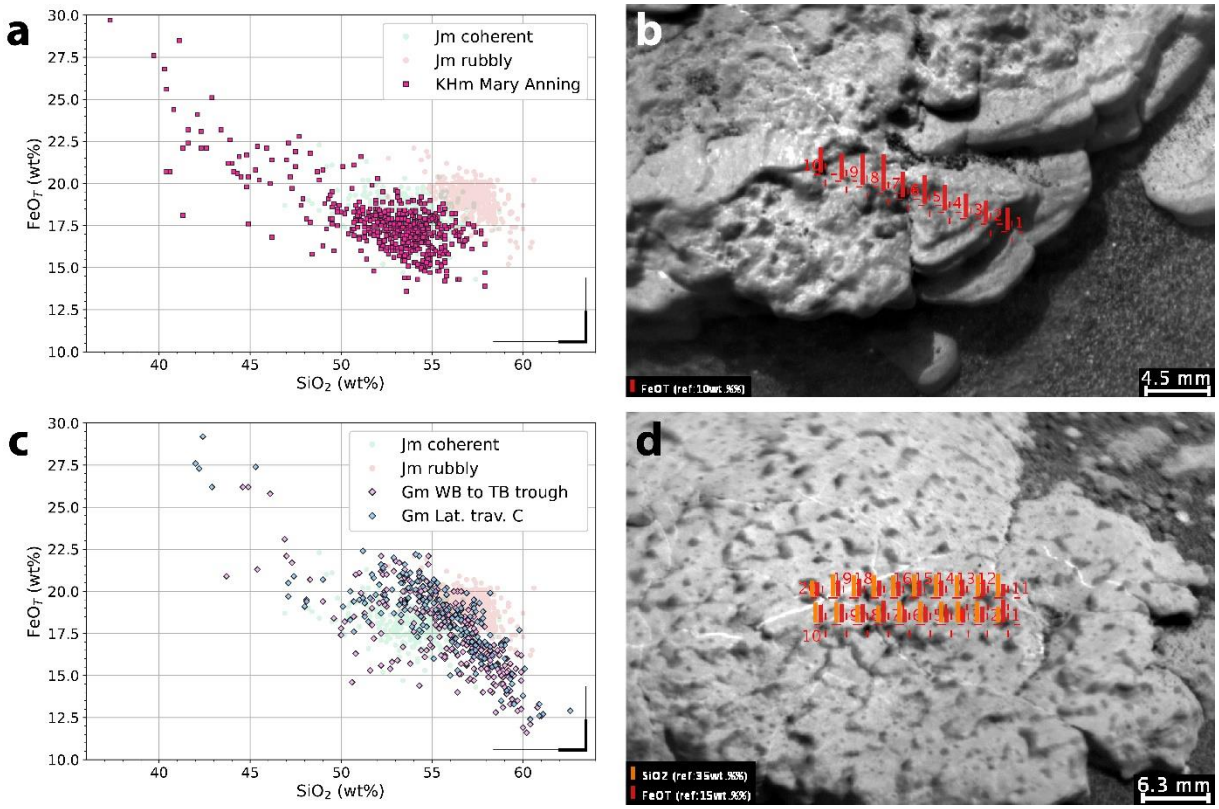


**Figure 5.** Iron variability observed in the Knockfarril Hill (KHm) and Glasgow (Gm) members. (a) $FeO_T$ vs $SiO_2$ plot for the bedrock of the Mary Anning area. The error bars in the lower right corner represent the accuracy (thin line) and precision (thick line) of the relevant oxides. (b) RMI image of target Formartine (sol 2867), which is located within the knobby-looking layer of the Mary Anning area where high-Fe points were identified. The red bars represent the $FeO_T$ abundances of each point of the raster. (c) $FeO_T$ vs $SiO_2$ plot for the bedrock analyzed in two areas of the Glasgow member (Lat. trav. C = Lateral traverse C; TB = Tower butte; WB = Western butte; see figure 1 for localizations). (d) RMI image of target Glenalmond (sol 2656), a bedrock slab with embedded dark-toned features located in the trough between Western butte and Tower butte. The orange and red bars represent the $SiO_2$ and $FeO_T$ abundances of each point of the raster. In the two left panels, Jura coherent and rubbly bedrock compositions are displayed as semi-transparent points for comparison.

**Table 2.** *Average chemical compositions of the Knockfarril Hill bedrock measured by ChemCam, in wt%.*

| Subset | N[a] | $SiO_2$ | $TiO_2$ | $Al_2O_3$ | $FeO_T$ | MgO | CaO | $Na_2O$ | $K_2O$ | MnO | Sum | CIA |
|---|---|---|---|---|---|---|---|---|---|---|---|---|
| Teal Ridge | 59 | 51.9 (2.2) | 1.02 (0.26) | 12.7 (1.9) | 19.1 (1.1) | 7.7 (0.8) | 2.9 (1.1) | 2.71 (0.39) | 0.86 (0.29) | 0.11 (0.04) | 99.01 (3.37) | 54.6 (4.4) |
| Harlaw Rise | 118 | 54.5 (1.7) | 1.01 (0.20) | 11.4 (1.2) | 19.0 (1.0) | 7.0 (1.1) | 1.8 (0.8) | 2.41 (0.26) | 1.45 (0.45) | 0.09 (0.11) | 98.58 (2.24) | 56.4 (3.3) |
| Glen Etive | 274 | 55.3 (1.4) | 0.99 (0.13) | 11.5 (1.1) | 18.8 (1.0) | 6.4 (0.5) | 1.7 (0.9) | 2.38 (0.29) | 1.89 (0.34) | 0.05 (0.04) | 99.05 (2.25) | 56.1 (3.3) |
| Rock Nab | 36 | 57.5 (0.8) | 1.03 (0.06) | 11.3 (0.7) | 20.1 (0.7) | 4.1 (0.3) | 1.1 (0.2) | 2.62 (0.13) | 1.98 (0.24) | 0.01 (0.01) | 99.62 (1.30) | 57.5 (1.7) |
| Mary Anning | 502 | 52.6 (3.3) | 0.92 (0.12) | 10.6 (1.2) | 17.6 (2.0) | 9.0 (1.6) | 1.7 (0.6) | 2.37 (0.24) | 0.95 (0.30) | 0.37 (0.67) | 96.19 (3.61) | 57.0 (2.5) |

*Note.* Standard deviations (1σ) are given in parentheses. See text for details about the subsets. [a]N = number of LIBS points used for the calculations.

### 3.3 The Buttes

On her way south toward the Greenheugh pediment, between sols 2564 and 2744, *Curiosity* successively visited Central butte, Western butte and Tower butte (locations #5, #6 and #7 in Figure 1). From a stratigraphic point of view, the northern flanks of the first two buttes encompass the contact between the Knockfarril Hill and Glasgow members (Figure 1; Bennett et al., this issue). However, the observed compositional variations do not strictly follow this stratigraphic boundary; from a geochemical point of view, it is therefore more useful to consider the Buttes as a whole, and separately from the rest of Glen Torridon.

The topographic ledge forming the base of Central butte (CB) on its northern side has a composition in family with the Jura and Knockfarril Hill members, and is most closely related to the rubbly endmember owing to its MgO, $K_2O$ and $SiO_2$ contents; however, its CaO abundance is variable, and slightly higher on average (1.9 wt%; Table 3). On the flank of Central butte, the compositions also fall within the range observed in the Jura and Knockfarril Hill members, but they are very variable—even between points from the same raster—and the average CaO content reaches 2.6 wt% (Table 3). Despite this variability, it is worth noting that $K_2O$ and $Na_2O$ remain well correlated with each other (Figure 6a). Lastly, the flank of Western butte (WB) is less heterogeneous, and displays compositions similar to the ledge of Central butte (Figure 6; Table 3).

A chemical shift is observed on the shoulder of Western butte (~7 m above the Knockfarril Hill-Glasgow contact), and becomes even more pronounced near the top (~11 m above the Knockfarril Hill-Glasgow contact). This shift mainly consists in an increase of the CaO content and a decrease of the $SiO_2$ content (Table 3). The sum of quantified oxides also decreases noticeably. In addition, the $K_2O$ abundances decrease while the $Na_2O$ abundances slightly increase, and the correlation between the two oxides thus essentially disappears (Figure 6a). As shown in Gasda et al. (this issue), this chemical shift occurs in an area where numerous diagenetic concretions are observed. However, the diagenetic features themselves are not responsible for the changes in composition described above, because the LIBS points that sampled them are excluded from the data set used here (see section 2.2); moreover, there is no significant difference in composition between the concretion-rich and concretion-free bedrock targets (see also Gasda et al., this issue).

After descending from Western butte, *Curiosity* traversed a shallow trough before ascending the flank of Tower butte (TB) toward the Siccar Point unconformity, which marks the base of the Greenheugh pediment capping unit (Figure S3). From the trough to the Hutton interval (defined as the interval of light-toned rocks just below the unconformity; Bennett et al., this issue), the measurements made by ChemCam show a repetition of the trends observed at Western butte (compare upper and lower panels of Figure 6).

Another distinctive characteristic of the Buttes is the high number of fluorine detections made by ChemCam—using the CaF molecular emission (Forni et al., 2015)—, in sharp contrast with the rest of Glen Torridon (Figure 7a). These detections mainly occur near the top of Western butte and on the bench feature on the flank of Tower butte where the Hutton drill hole is located (Figures 1 and S3). Interestingly, F is detected in both the bedrock (~0.4 wt% on average) and the diagenetic features (~1.0 wt% or more depending on the type of feature; Gasda et al., this issue). In the bedrock targets, the shot-to-shot variations of F abundance are well correlated with those of Ca; in addition, P emission lines are sometimes present (e.g., target Ben_Wyvis, sol 2738). Together, these two observations make

fluorapatite the most likely F-bearing phase, in agreement with the identification of apatite by the CheMin instrument at the Hutton drill hole (Figure 7b) (Thorpe et al., this issue).

Overall, the bedrock near the top of Western Butte and just below the Siccar Point unconformity at Tower Butte can be considered as "anomalous" compared to the rest of the Glen Torridon region. It is characterized by a weak positive correlation between MgO and $K_2O$ (Pearson coefficient: +0.41; Table S5), instead of a negative one elsewhere, and a decorrelation between $K_2O$ and $Na_2O$ (Pearson coefficient: -0.04) compared to a weak correlation elsewhere in the Glasgow member (Pearson coefficient: +0.50; Table S6). Finally, while the average CIA values remain elevated in the low parts of the Buttes (~54-56), they drop to ~44 near the top of Western butte and in the Hutton interval. In comparison, the eolian sandstones exposed on top of the Greenheugh pediment, which belong to the younger Stimson formation (Figures 1 and S1), have an average CIA value of ~39 (Table 3).

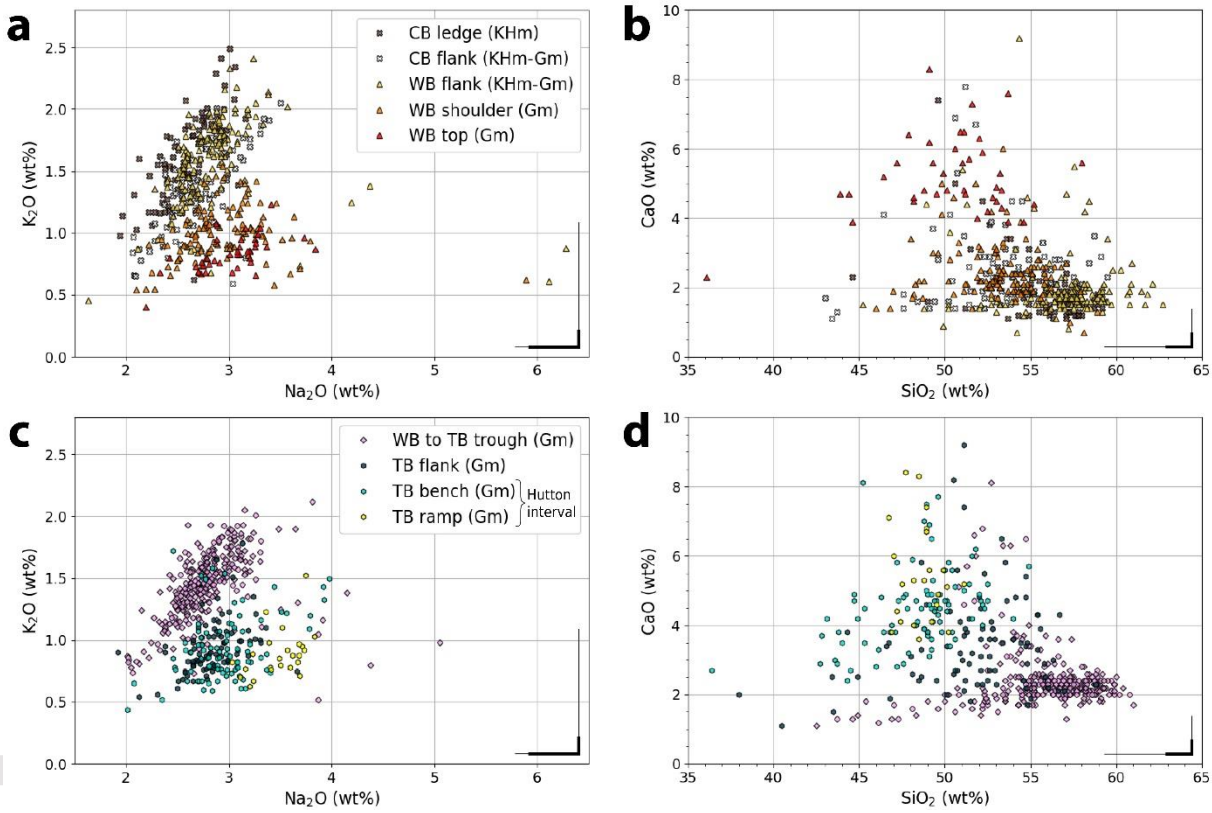


**Figure 6.** Major-element oxide compositions of the Buttes bedrock (CB = Central butte; TB = Tower butte; WB = Western butte). $K_2O$ vs $Na_2O$ and CaO vs $SiO_2$ plots for CB and WB (a, b) and for TB (c, d). The error bars in the lower right corner of each plot represent the accuracy (thin line) and precision (thick line) of the relevant oxides. Each symbol corresponds to a single LIBS point and is color-coded according to the geographic location (see legends in panels a and c). The "TB bench" is the flatter area near the top of Tower butte where *Curiosity* collected the Hutton drill sample (see Figure S3); the "TB ramp" is the slope above the bench that the rover used to ascend onto the Greenheugh pediment—thus, these targets are even closer to the Siccar Point unconformity than those of the bench. The bench and ramp are regrouped under the name "Hutton interval" in Table 3.

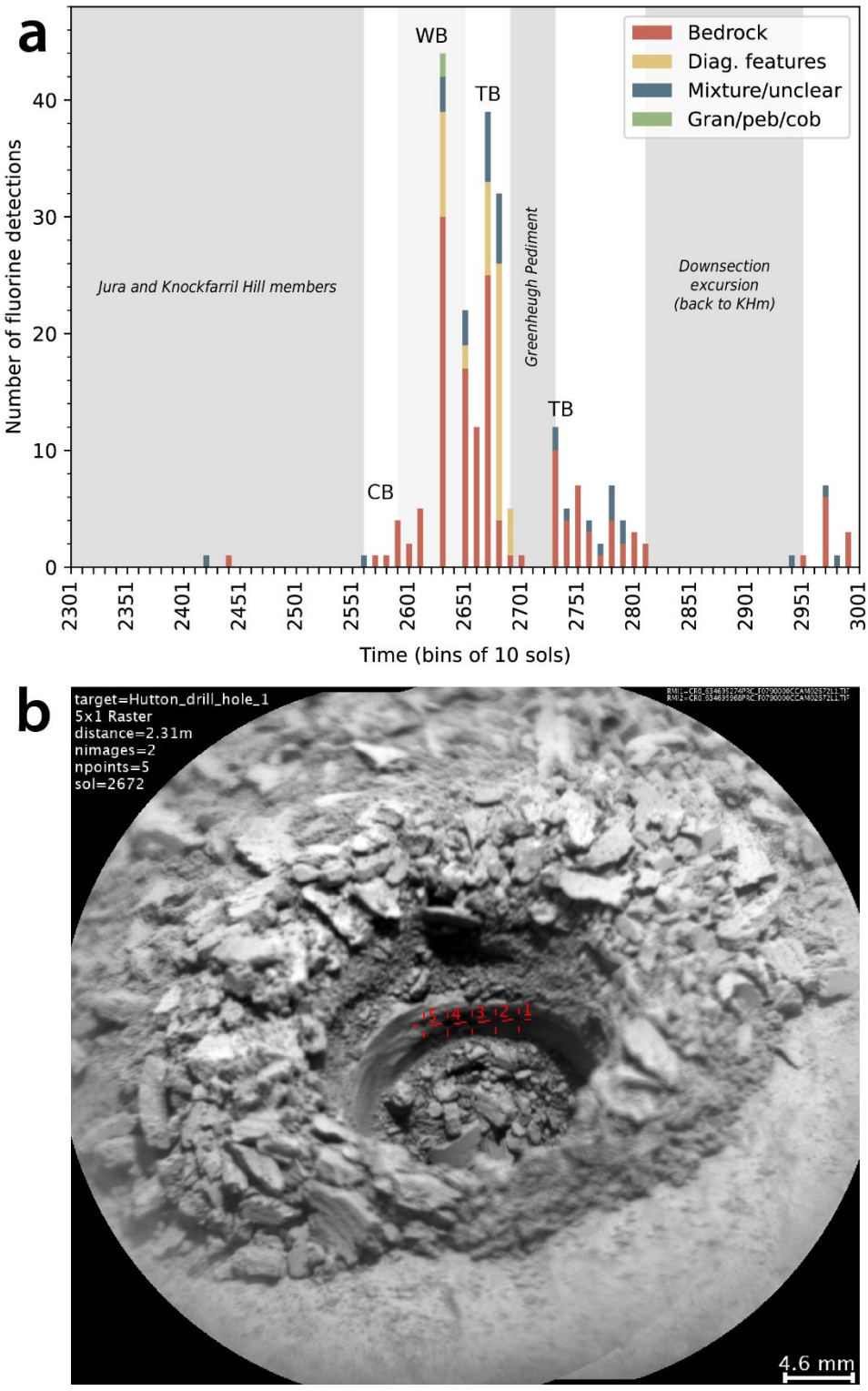


**Figure 7.** Fluorine detections by ChemCam in Glen Torridon. (a) Number of fluorine detections as a function of time during the entire GT campaign, grouped in bins of 10 sols (CB = Central butte; TB = Tower butte; WB = Western butte). One detection is defined as a LIBS point with a predicted F content >0.2 wt%. Colors indicate the type of target (Diag. features = diagenetic features; Gran/peb/cob = granules, pebbles or cobbles). (b) RMI documentation of a LIBS raster performed on the wall of the Hutton drill hole on sol 2672. Fluorine was detected in all 5 points.

**Table 3.** *Average chemical compositions of the Buttes bedrock measured by ChemCam, in wt%.*

| Subset | N[a] | $SiO_2$ | $TiO_2$ | $Al_2O_3$ | $FeO_T$ | MgO | CaO | $Na_2O$ | $K_2O$ | MnO | Sum | CIA |
|---|---|---|---|---|---|---|---|---|---|---|---|---|
| CB ledge | 77 | 55.7 (2.5) | 0.96 (0.09) | 11.6 (1.1) | 19.5 (1.3) | 5.0 (0.6) | 1.9 (1.0) | 2.59 (0.28) | 1.61 (0.37) | 0.03 (0.02) | 98.80 (3.03) | 55.4 (4.4) |
| CB flank | 82 | 53.1 (3.3) | 0.96 (0.13) | 12.2 (1.6) | 19.4 (2.3) | 6.0 (1.2) | 2.6 (1.2) | 2.70 (0.33) | 1.36 (0.34) | 0.04 (0.01) | 98.41 (4.00) | 53.7 (4.5) |
| WB flank | 146 | 56.7 (2.8) | 0.99 (0.09) | 12.5 (1.3) | 18.2 (2.2) | 4.7 (1.1) | 2.0 (1.0) | 2.85 (0.51) | 1.57 (0.34) | 0.03 (0.03) | 99.57 (3.17) | 55.6 (3.9) |
| WB shoulder | 115 | 53.1 (2.5) | 0.99 (0.11) | 12.1 (1.3) | 19.7 (1.4) | 5.1 (0.9) | 2.4 (0.8) | 2.93 (0.44) | 1.00 (0.21) | 0.05 (0.02) | 97.35 (3.47) | 54.0 (4.1) |
| WB top | 39 | 50.4 (3.8) | 0.92 (0.05) | 12.2 (1.4) | 19.0 (3.3) | 5.3 (1.0) | 5.2 (1.1) | 3.03 (0.33) | 0.83 (0.15) | 0.12 (0.04) | 96.90 (3.11) | 44.3 (3.5) |
| WB-TB trough | 299 | 55.7 (3.1) | 0.99 (0.08) | 12.3 (1.5) | 17.6 (2.5) | 4.5 (0.6) | 2.4 (0.9) | 2.80 (0.43) | 1.44 (0.27) | 0.03 (0.02) | 97.79 (3.43) | 54.0 (3.7) |
| TB flank | 86 | 51.6 (3.6) | 0.92 (0.09) | 11.8 (1.4) | 18.6 (3.3) | 5.2 (1.9) | 3.5 (1.4) | 2.83 (0.27) | 0.94 (0.21) | 0.11 (0.24) | 95.52 (3.77) | 50.1 (4.5) |
| Hutton interval | 113 | 48.5 (2.6) | 0.91 (0.10) | 11.5 (1.5) | 19.4 (1.8) | 5.4 (1.4) | 4.7 (1.3) | 3.15 (0.92) | 0.92 (0.26) | 0.11 (0.03) | 94.54 (3.74) | 44.1 (4.0) |
| GP Stimson | 375 | 43.2 (3.5) | 0.93 (0.20) | 9.2 (2.6) | 20.6 (3.2) | 8.2 (2.7) | 5.3 (2.6) | 2.77 (0.73) | 0.54 (0.25) | 0.26 (0.51) | 90.96 (3.63) | 38.8 (7.6) |

*Note.* Standard deviations (1σ) are given in parentheses. See text for details about the subsets (CB = Central butte; TB = Tower butte; WB = Western butte). The composition of the Stimson bedrock on top of the Greenheugh pediment (GP) is provided for comparison.
[a]N = number of LIBS points used for the calculations.

### 3.4 Glasgow member

The Glasgow member (Gm) overlies the Knockfarril Hill member and is the highest of the three stratigraphic members exposed in Glen Torridon (Figures 1 and S1; Bennett et al., this issue). As mentioned previously, a large part of the Buttes belongs to the Glasgow member, but in this section we focus on the Glasgow bedrock away from the Buttes.

After leaving the Glasgow drill site, *Curiosity* drove mostly eastward and at low angle with respect to the contour lines—the absolute elevation gain was only ~22 meters between sols 2780 and 3007. Here, in order to evaluate the lateral variability of the Glasgow member, we divide this lateral traverse into four sections, labeled A to D in Figure 1.

Although no bedrock target from the Glasgow member was classified as "rubbly" based on its outcrop expression, the measured compositions span the two geochemical endmembers defined by the coherent and rubbly bedrock types of the Jura member. The MgO content, in particular, displays significant lateral variations (Figure 8a; Table 4): it is as low as 3.2 wt% in section B of the lateral traverse (just east of Bloodstone hill—location #8 in Figure 1), but increases in section C (i.e., after the downsection excursion into the Knockfarril Hill member) and finally reaches 5.9 wt% in the area of rougher terrain mapped as "Polygonally fractured unit c" by Hughes (2021)—location #10 in Figure 1. The $K_2O$ content also varies laterally (average values range from 1.01 to 1.67 wt%; Table 4), but the pattern is different than for MgO, with no obvious change between the west side and the east side of the lateral traverse (Figure 8b).

The most distinctive feature of the Glasgow bedrock is the large variability of $FeO_T$ at the scale of a LIBS raster—i.e., a few millimeters to centimeters. On Figure 8c, one can clearly see that the dispersion of $FeO_T$ values is much lower in the Knockfarril Hill member (setting aside the Fe-rich, knobby-looking layer mentioned in section 3.2), and re-increases upon return to the Glasgow member. This greater variability coincides with the appearance of millimeter-sized dark-toned features embedded in the bedrock, likely of diagenetic origin (Gasda et al., this issue), which are enriched in $FeO_T$ and depleted in $SiO_2$ (Figure 5c-d).

Conversely, the LIBS points in between the darked-toned features are low in $FeO_T$ (down to ~12 wt%) and slightly enriched in $SiO_2$. The lowest $FeO_T$ abundances (down to 6.5 wt%) of the entire Glasgow bedrock were measured on the flank of Bloodstone hill (Figure 8c); however, this outcrop may be slightly anomalous owing to its light-toned appearance (see location #8 in Figure 1) and its lower CIA compared to the adjacent terrains (Table 4).

Besides the negative correlation between $FeO_T$ and $SiO_2$ (Pearson coefficient: -0.75; Table S6), the Glasgow bedrock is characterized by a positive correlation between $SiO_2$ and $Al_2O_3$ (+0.67). The negative correlation between MgO and $K_2O$ observed in the Jura and Knockfarril Hill members (Tables S3 and S4) essentially disappears in Glasgow (-0.10). A weak positive correlation between $SiO_2$ and $K_2O$ (+0.48) remains, but it is much less pronounced than in Jura and Knockfarril Hill. Finally, with the exception of the flank of Bloodstone hill, the average CIA values are almost as elevated (~54-56) as in the Knockfarril Hill member (Tables 2 and 4).

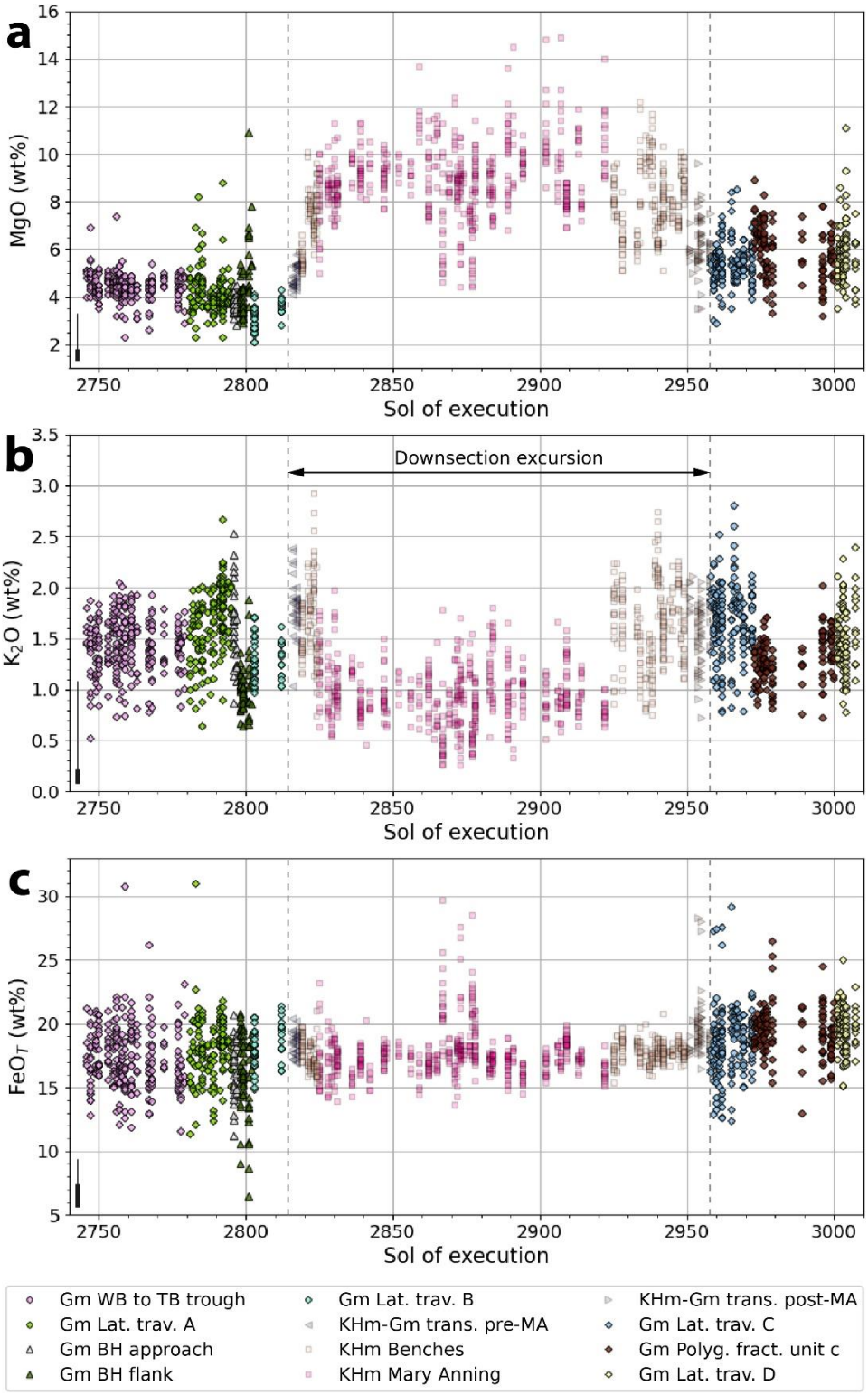


**Figure 8.** Variations in MgO (a), $K_2O$ (b) and $FeO_T$ (c) abundances along the eastward traverse within the Glasgow member (Gm). Data acquired during the downsection excursion into the Knockfarril Hill member (KHm) are also shown for comparison (symbols with reduced opacity between the dashed lines). The x axis corresponds to time of measurement and does not reflect horizontal distance (see Figure 1 for localization). BH = Bloodstone hill; Lat. trav. = lateral traverse; MA = Mary Anning; Polyg. fract. unit c = Polygonally fractured unit c (Hughes, 2021); TB = Tower butte; trans. = transition; WB = Western butte. The error

bars in the lower left corner of each plot represent the accuracy (thin line) and precision (thick line) of the relevant oxides.

**Table 4.** *Average chemical compositions of the Glasgow bedrock measured by ChemCam, in wt%.*

| Subset | N* | $SiO_2$ | $TiO_2$ | $Al_2O_3$ | $FeO_T$ | MgO | CaO | $Na_2O$ | $K_2O$ | MnO | Sum | CIA |
|---|---|---|---|---|---|---|---|---|---|---|---|---|
| WB-TB trough | 299 | 55.7 (3.1) | 0.99 (0.08) | 12.3 (1.5) | 17.6 (2.5) | 4.5 (0.6) | 2.4 (0.9) | 2.80 (0.43) | 1.44 (0.27) | 0.03 (0.02) | 97.79 (3.43) | 54.0 (3.7) |
| Lateral traverse A | 142 | 55.0 (2.7) | 1.00 (0.06) | 12.4 (1.3) | 18.1 (2.4) | 4.2 (0.9) | 2.0 (0.5) | 2.87 (0.28) | 1.65 (0.34) | 0.03 (0.01) | 97.33 (3.02) | 55.1 (2.2) |
| BH flank | 58 | 55.9 (2.4) | 1.08 (0.10) | 13.3 (1.3) | 15.9 (3.1) | 4.4 (1.4) | 3.6 (1.5) | 2.91 (0.30) | 1.01 (0.23) | 0.05 (0.03) | 98.11 (1.58) | 52.0 (4.4) |
| Lateral traverse B | 43 | 55.5 (2.0) | 1.05 (0.09) | 12.7 (1.2) | 18.4 (1.6) | 3.2 (0.5) | 2.4 (0.8) | 2.85 (0.23) | 1.31 (0.20) | 0.02 (0.01) | 97.36 (3.57) | 55.0 (3.3) |
| Lateral traverse C | 177 | 55.0 (3.5) | 0.97 (0.06) | 11.7 (1.4) | 18.6 (2.6) | 5.4 (0.9) | 1.5 (0.3) | 2.72 (0.25) | 1.67 (0.35) | 0.09 (0.23) | 97.66 (3.80) | 56.3 (1.8) |
| Polyg. fract. unit c | 131 | 52.8 (2.9) | 0.97 (0.08) | 11.2 (1.2) | 19.4 (1.9) | 5.9 (1.1) | 1.8 (0.8) | 2.52 (0.20) | 1.30 (0.23) | 0.09 (0.02) | 96.04 (3.45) | 56.0 (3.8) |
| Lateral traverse D | 90 | 53.6 (2.6) | 0.96 (0.07) | 11.3 (1.2) | 19.6 (1.7) | 5.8 (1.2) | 1.5 (0.4) | 2.63 (0.23) | 1.50 (0.32) | 0.19 (0.70) | 97.13 (3.86) | 56.5 (1.9) |

*Note.* Standard deviations (1σ) are given in parentheses. See text for details about the subsets (BH = Bloodstone hill; TB = Tower butte; WB = Western butte).
[a]N = number of LIBS points used for the calculations.

## 4 Discussion

### 4.1 Synthesis of results

The continuous survey of the bedrock by ChemCam along the Glen Torridon traverse has enabled the identification of four main types of compositions (Figure 9).

The first two types are associated with the main outcrop expressions found in the Jura and Knockfarril Hill members: coherent and rubbly (respectively Type 1 and Type 2). Compared to typical Murray formation bedrock observed earlier in the mission (Frydenvang et al., 2020), the rubbly bedrock has an homogeneous composition characterized by low MgO (4.5—5.3 wt%, first and third quartiles), and elevated $K_2O$ (1.7—2.1 wt%) and $SiO_2$ (56.3—57.7 wt%). The coherent bedrock is more variable from one location to another (Table 2), but has generally higher MgO (6.3—8.5 wt%), and lower $K_2O$ (0.9—1.7 wt%) and $SiO_2$ (52.9—55.7 wt%).

Type 3 corresponds to the baseline Glasgow bedrock, i.e., away from the Buttes. It is overall similar to Type 1, but with a MgO content more in line with Type 2 (4.2—5.5 wt%, first and third quartiles). It is also characterized by the higher variability in $SiO_2$ and $FeO_T$ abundances (see expanded whiskers in boxplots of Figure 9a-b), although the average values are in line with those of both Type 1 and Type 2.

Lastly, Type 4 is only found in the Buttes subregion, near the top of Western butte and in the Hutton interval, i.e., just below the Siccar Point unconformity in the Tower butte area. It is mainly characterized by elevated CaO (4.0—5.6 wt%, first and third quartiles; compared to 1.3—2.0 wt% in the rest of Glen Torridon), as well as low $SiO_2$ and low sum of oxides (Figure 9a,f).

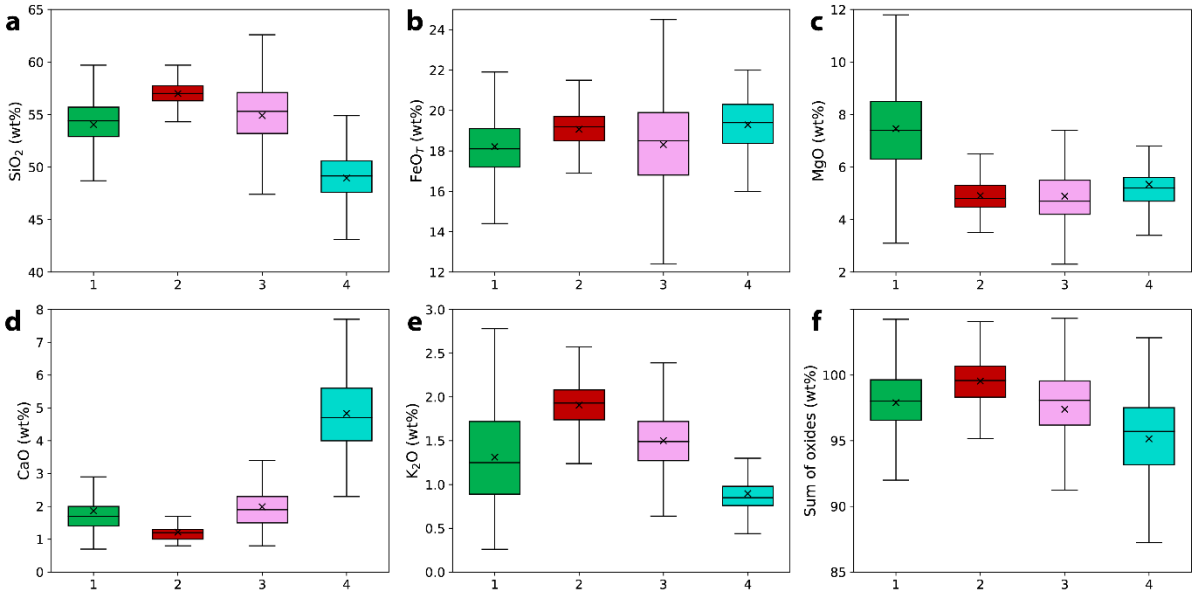


**Figure 9.** The four main types of bedrock composition found in Glen Torridon (numbered along the x axis), for selected oxides. See Figure S4 for $TiO_2$, $Al_2O_3$, $Na_2O$ and MnO. Type 1: coherent bedrock of the Jura and Knockfarril Hill members; Type 2: rubbly bedrock of the Jura and Knockfarril Hill members; Type 3: baseline Glasgow member bedrock; Type 4: anomalous Glasgow bedrock (top of Western butte and Hutton interval). The boxplots show the first (Q1) and third (Q3) quartiles (the box itself), the median (the line inside the box), and the mean (the x symbol) of the data. The lower whisker extends to the lowest value above Q1–1.5*(Q3–Q1), and the upper whisker extends to the highest value below Q3+1.5*(Q3–Q1). For clarity, outliers are not displayed.

### 4.2 Chemistry vs mineralogy

In this section, we compare the chemical measurements from ChemCam with the mineralogy of the Glen Torridon drill samples determined by the CheMin X-ray diffractometer (Thorpe et al., this issue).

The Aberlady (AL), Kilmarie (KM), Glen Etive (GE), Glen Etive 2 (GE2), Mary Anning (MA), Mary Anning 3 (MA3) and Groken (GR) drill samples have all been extracted from coherent bedrock slabs within the Jura and Knockfarril Hill members. Therefore, they all belong to the Type 1 composition defined above, even though there is some variability from one location to another, as detailed previously (Tables 1 and 2). CheMin analyses show that these samples are also in family from a mineralogical point of view, with the dominant components being plagioclase, phyllosilicates (mainly ferric smectites) and X-ray amorphous materials (Thorpe et al., this issue). Several of these samples also have in common that they contain mineral phases detected for the first time in the mission: siderite in KM, GE and MA3 (and possibly in MA and GR, but near detection limit); and a putative mixed-layer phyllosilicate characterized by a main diffraction peak at 9.22 Å in KM, MA, MA3 and GR (Bristow et al., 2021; Thorpe et al., this issue).

In addition, and as the name suggests, the Glasgow drill sample (GG) was collected within the Glasgow member, more precisely in the trough separating Western butte and Tower butte (Figure 1). From a ChemCam perspective, the Glasgow bedrock has an average composition in line with the rest of Glen Torridon, but a larger variability in $SiO_2$ and $FeO_T$ abundances (Figure 9, Type 3). This variability is likely an effect of a diagenetic overprint,

since this type of composition is associated with the appearance of widespread dark-toned features enriched in $FeO_T$ (Figure 5c-d; see also Gasda et al., this issue). The CheMin results also place the GG sample in family with the rest of Glen Torridon, but with an increased amount of hematite and a reduced amount of phyllosilicates (Thorpe et al., this issue).

Lastly, the Hutton drill sample (HU) was collected near the top of Tower butte, just ~3 m below the Siccar Point unconformity. This location corresponds to a distinct bedrock composition in ChemCam data (Type 4 defined above), which we consider as anomalous given the higher CaO abundances, the lower $SiO_2$ abundances, and the numerous fluorine detections. The CheMin analysis of the HU sample shows that it is also anomalous from a mineralogical point of view. Specifically, this sample has much less phyllosilicates, and is the only one in Glen Torridon to contain significant amounts of magnetite, apatite, cristobalite and opal-CT (Thorpe et al., this issue). The identification of apatite by CheMin agrees well with the fluorine detections from ChemCam, which are correlated with Ca on a shot-to-shot basis, and are sometimes accompanied by P detections. The identification of silica polymorphs, on the other hand, may seems at odds with the lower $SiO_2$ abundances measured by ChemCam in Type 4 targets (Figure 9a); however, the silica forming the cristobalite and opal-CT may come from the destabilization of pre-existing silicate phases rather than representing an addition of silica in the system (see section 4.5.2).

Another important aspect of the comparison between chemistry and mineralogy is the correlation between the Chemical Index of Alteration (CIA) and the amount of clay minerals. The latter can form in relatively high abundances without an increase of the CIA. For example, in the Sheepbed mudstone on Aeolis Palus, the lack of correlation between CIA and clay minerals indicates that the alteration occurred in a closed system, with no significant loss of soluble elements (McLennan et al., 2014; Vaniman et al., 2014). In contrast, an open-system type of alteration is favored in the Murray formation, where the CIA values and the amount of clay minerals have both been observed to gradually increase up-section (Bristow et al., 2018; Mangold et al., 2019; Rampe et al., 2017), except on Vera Rubin ridge, where the original mineralogy has been modified by enhanced diagenesis (Fraeman et al., 2020; Rampe et al., 2020). Figure 10 shows the CIA values measured by ChemCam in Glen Torridon and the clay mineral abundances found by CheMin in the drill samples from the corresponding areas (for example, the CIA value of the Glen Etive area, taken from Table 2, is compared to the mineralogy of the GE and GE2 samples). Setting aside the anomalous HU sample (discussed in section 4.5.2), the Glen Torridon bedrock displays elevated CIA values compared to potential source rocks, and has among the highest clay mineral abundances found at Gale crater (Thorpe et al., this issue). Such a combination of high CIA values and abundant clay minerals suggests that the latter were formed by aqueous alteration with a sufficiently high water-to-rock ratio to remove some of the mobile elements from the sediments.

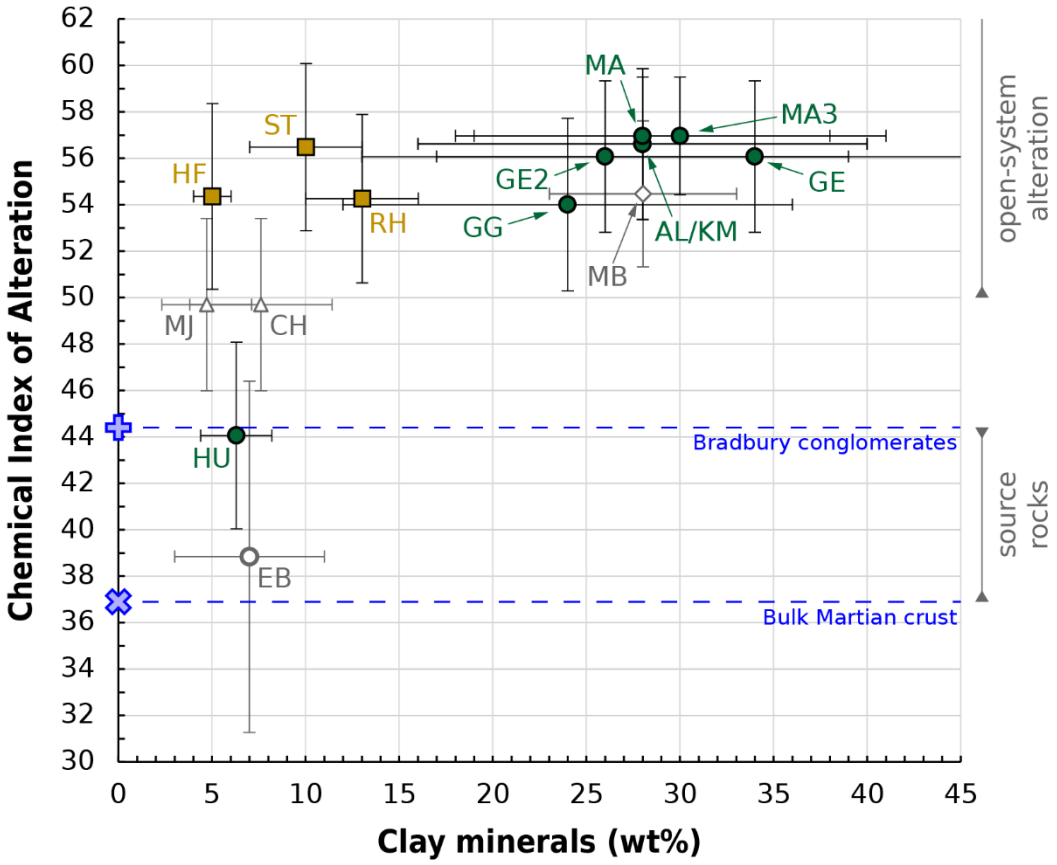


**Figure 10**. CIA measured by ChemCam versus clay minerals found by CheMin in drill samples from Glen Torridon. The vertical error bars represent the standard deviation of the CIA values (Tables 1-4); whereas the horizontal error bars correspond to the uncertainties reported by the CheMin team. The Glen Torridon samples (AL, KM, GE, GE2, HU, GG, MA and MA3) are shown with green circles. Other samples from Gale crater are shown for comparison: Edinburgh (EB), which was collected in the Stimson formation on top of the Greenheugh pediment (Bedford et al., this issue); Stoer (ST), Highfield (HF) and Rock Hall (RH), which were collected on Vera Rubin ridge (Frydenvang et al., 2020; Rampe et al., 2020); Marimba (MB), which was collected in the Karasburg member (Bristow et al., 2018; Frydenvang et al., 2020); Confidence Hills (CH) and Mojave 2 (MJ), which were collected at Pahrump Hills, the lowest exposed section of the Murray formation (Frydenvang et al., 2020; Rampe et al., 2017). Two proxies for the source rocks of the sediments are also shown: the mean composition of the Bradbury conglomerates (a good proxy for the regional crust composition; Mangold et al., 2016) and the estimated bulk composition of the Martian crust (Taylor & McLennan, 2009). Note that the clay content of the Bradbury conglomerates is not known with certainty and could be non-zero.

### 4.3 Origin of the magnesium enrichment in the coherent bedrock

One of the most striking geochemical observations of the Glen Torridon campaign is the difference in composition between the coherent and rubbly bedrock exposed in the Jura and Knockfarril Hill members (Figure 2c). As noted previously, several drill samples were taken from coherent bedrock slabs; therefore, we can use the CheMin results to investigate the possible origin of the MgO enrichment observed by ChemCam.

The two most abundant crystalline phases identified by CheMin in the coherent bedrock are plagioclase and phyllosilicates (Thorpe et al., this issue). Plagioclase does not

contain Mg, and thus cannot account for the observed enrichment. On the other hand, phyllosilicates can be Mg-bearing. The main phyllosilicate phase present in Glen Torridon is a dioctahedral $Fe^{3+}$-smectite close to nontronite (Thorpe et al., this issue), thus a Mg-poor species. However, CheMin detected what is likely a second phyllosilicate phase, characterized by a diffraction peak at 9.22 Å. Bristow et al. (2021) and Thorpe et al. (this issue) have interpreted this phase as a mixed-layer phyllosilicate, composed of talc/minnesotaite and minor serpentine or greenalite. The precise composition of this phase is not known, but since talc is a Mg-rich mineral (formula: $Mg_3Si_4O_{10}(OH)_2$), we investigated whether it could explain the observed MgO enrichment.

Figure 11 illustrates the results of a simple mixing model between the average of Types 1 and 2 bedrock targets (see section 4.1) and a pure talc/minnesotaite phase. Although a ratio of ~10% talc / 90% minnesotaite could produce a trend consistent with the observations on the MgO vs $SiO_2$ diagram (dashed gray line in Figure 11a), the rock would have to be almost completely composed of this phase in order to approach the average composition of the Jura coherent bedrock, and stronger MgO enrichments measured on individual LIBS points (Figure 2a; Figure 4c) would be unreachable. Moreover, on the $FeO_T$ vs $SiO_2$ diagram, no ratio of talc and minnesotaite can produce a trend consistent with the observations (Figure 11b). Therefore, we can conclude that the mixed-layer phyllosilicate found by CheMin is unlikely to be the source of the MgO enrichment measured by ChemCam. Similar arguments can made regarding other silicate phases such as pyroxenes.

Another hypothesis is that the MgO enrichment is due to a non-silicate phase at or below the detection limit of CheMin, or X-ray amorphous. In particular, Mg-sulfates have been identified *in situ* lower in the Murray formation (Rapin et al., 2019), and orbital data suggest that they are present in the "sulfate-bearing unit", stratigraphically above Glen Torridon (Fraeman et al., 2016; Milliken et al., 2010). Figure 11 shows that the addition of a small amount of Mg-sulfate can create a trend reasonably consistent with the MgO enrichment of the coherent bedrock. The sulfur signal measured by ChemCam is also compatible with this interpretation (Figure S5). Although modeled as the monohydrated species kieserite in Figure 11, the Mg-sulfate phase could be polyhydrated (e.g., epsomite, hexahydrite, meridianiite), or could consist of a combination of several species. In turn, polyhydrated Mg-sulfates may be difficult to detect with CheMin because their rapid dehydration inside the instrument is likely to make them X-ray amorphous (Vaniman et al., 2018; Vaniman & Chipera, 2006). If the Mg-sulfate hypothesis is correct, they may have been deposited by concentrated fluids percolating through the sediments during early diagenesis (Rapin et al., 2019). Percolation would have been favored by the higher porosity of the coherent bedrock compared to the rubbly bedrock (Caravaca et al., this issue), hence explaining the observed MgO enrichment in the former.

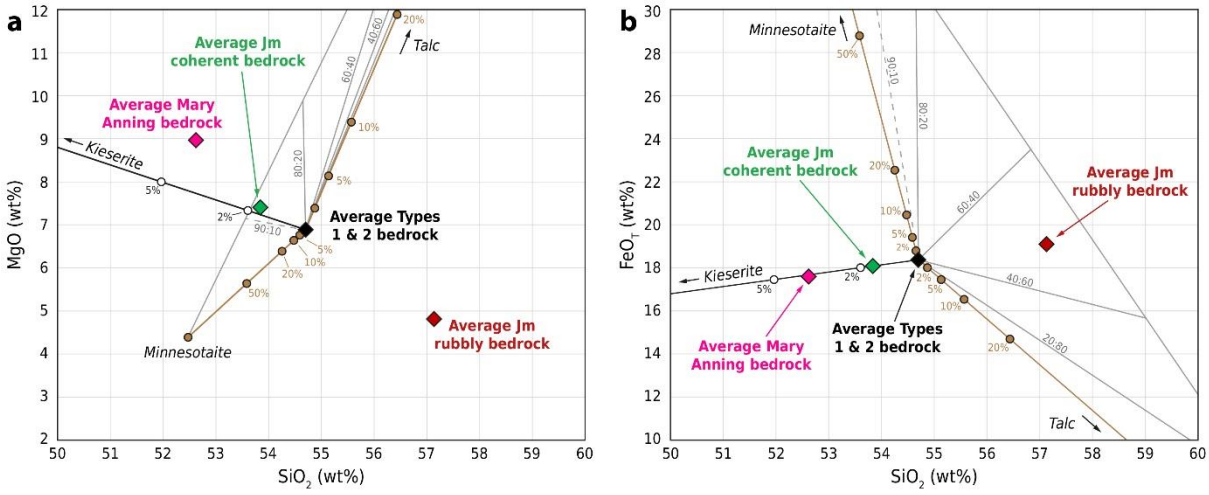


**Figure 11**. Mixing model between the average Types 1 and 2 bedrock targets (black diamond) and a pure talc/minnesotaite phase (brown and gray lines), or pure kieserite (black line). The average compositions of the coherent and rubbly endmembers as observed in the Jura member are shown for comparison (green and red diamonds), as well as the average composition of the Mg-rich bedrock of the Mary Anning area (pink diamond).

4.4 Origin of the potassium enrichment in the rubbly bedrock

Due to the small size of the individual blocks forming the rubbly bedrock, it was not possible to collect a drill sample from it, and thus not possible to analyze it with CheMin. Nonetheless, the rubbly bedrock is an important geochemical endmember as it is the spatially dominant component of the Jura member (Figure 2c), and thus the main contributor to the spectral signatures observed from orbit over the northern part of Glen Torridon. In this section, we investigate the possible mineralogy of the rubbly bedrock based on the geochemical measurements from ChemCam.

The rubbly bedrock is mainly characterized by enrichments in both $K_2O$ and $SiO_2$ (Table 1), which suggests the presence of a K-bearing silicate phase—a non-silicate phase such as jarosite would not account for the elevated $SiO_2$ content. Elevated $K_2O$ abundances were previously observed in the Kimberley formation (Le Deit et al., 2016), where CheMin XRD data showed an associated enrichment in sanidine (Treiman et al., 2016). The presence of K-feldspars was also inferred from ChemCam measurements in a group of Aeolis Palus rocks classified as trachytes (Cousin et al., 2017b; Sautter et al., 2015). On the other hand, a gradual enrichment in $K_2O$ with increasing CIA values was observed by Mangold et al. (2019) in ChemCam data from the lower Murray formation (Pahrump Hills to Sutton Island members; Figure 12), and was hypothesized to reflect a contribution from illite or a mixed-layer illite/smectite phase. The fact that the $K_2O$ enrichment coincides with a distinct outcrop expression in Glen Torridon provides an opportunity to re-evaluate this hypothesis.

Several lines of evidence argue against sanidine or another K-rich feldspar being responsible for the elevated $K_2O$ abundances measured in the rubbly bedrock. First of all, the shot-to-shot K/Al ratio never reaches the range that would be unambiguously indicative of K-feldspars (Text S2; Figure S6)—although this could be due to the laser beam always sampling some coexisting plagioclase crystals in these fine-grained rocks, resulting in intermediate K/Al values being measured in all shots. Second, the K/Rb ratio of the rubbly bedrock is lower than in the feldspar-rich targets of Aeolis Palus, and thus not consistent with an igneous contribution (Text S2; Figure S7). Third, Li and Cr are more abundant in the rubbly bedrock

than in the feldspar-rich targets—including the plagioclase-rich ones, thus ruling out a mixing effect in this case (Figure S7).

Conversely, Li and Cr are two elements known to get adsorbed onto clay minerals, and Li can also be present in their structure, substituting for K (e.g., Ajouyed et al., 2011; Williams & Hervig, 2005). In fact, at Gale crater, Li abundances measured by ChemCam have been shown to correlate well with the amount of clay minerals found by CheMin (Bristow et al., 2021; Frydenvang et al., 2020). Therefore, the elevated abundances of Li and Cr in the rubbly bedrock compared to the feldspar-rich targets of Aeolis Palus (Figure S7) is suggestive of a high amount of clay minerals in the former. Moreover, the CIA values measured in the rubbly bedrock are as high as those measured in the coherent bedrock (Table 1), which suggests that both endmembers have been aqueously altered to roughly the same degree.

Although the rubbly bedrock was not analyzed by CheMin, we have shown that the $K_2O$ content of the coherent bedrock is variable in the Jura and Knockfarril Hill members (Figure 9e). In particular, the average $K_2O$ abundance of the Glen Etive coherent bedrock (1.89 wt%; Table 2) is close to the one of the Jura rubbly bedrock (1.91 wt%; Table 1). Therefore, we can use the mineralogy of the GE and GE2 drill samples as a proxy for the rubbly bedrock, even though their overall chemical composition is not completely equivalent (e.g., the rubbly bedrock is Mg-poor compared to Glen Etive). The average $K_2O$ content in the Glen Etive area is 0.90 wt% higher than in the coherent bedrock of the Jura member, in which the Aberlady and Kilmarie samples were collected—the difference is essentially the same (0.91 wt%) if only the LIBS measurements inside the drill holes are considered. The increase in $K_2O$ would translate into 7.0 wt% sanidine (considering a typical formula of $K_{0.75}Na_{0.25}AlSi_3O_8$), an amount that would be easily detectable by CheMin for such a crystalline phase, but that is not observed (Bristow et al., 2021; Thorpe et al., this issue). On the other hand, the amount of illite needed to account for the difference in $K_2O$ would be higher than for sanidine—e.g., 8.6 wt% using the formula $K_{0.88}Al_2(Si_{3.12}Al_{0.88})O_{10}(OH)_2$ (Rosenberg, 2002). However, illite is poorly-crystalline, and can be difficult to distinguish from collapsed smectite under the low humidity conditions inside the CheMin instrument, especially if the two species are present as a mixed-layer phase (Thorpe et al., this issue).

Based on all the above observations, we conclude that the $K_2O$ enrichment of the rubbly bedrock is best explained by the presence of illite or a mixed-layer illite/smectite phase. On Earth, illitization tends to increase with temperature, and thus depth of burial (e.g., Pollastro, 1993; Velde & Vasseur, 1992). The strata examined by *Curiosity* in Glen Torridon have undoubtedly been buried under hundreds to thousands of meters of overlying sediments, the erosion of which has created the present-day topography of Aeolis Mons (Grotzinger et al., 2015; Le Deit et al., 2013; Thomson et al., 2011). Therefore, burial diagenesis is a plausible mechanism for the formation of illite at the expense of smectite within Gale crater, i.e., after sediment deposition (Borlina et al., 2015; Thorpe et al., this issue). However, in the Murray formation, $K_2O$ abundances vary with elevation (Frydenvang et al., 2020), and thus do not correlate with depth of burial; moreover, the rubbly bedrock of Glen Torridon, which belongs to the topmost member of the Murray formation, also represent the most homogeneous K-rich endmember so far (Figure 12). One possibility to explain this observation is that illite is a detrital phase; in this scenario, the $K_2O$ enrichment of the rubbly bedrock would be due to the deepest, most illite-rich rocks of the source region being exhumed last, and the resulting sediments being deposited toward the top of the sequence.

Illite being a detrital phase may also help to explain the contrasted composition of the adjacent rubbly (K-rich) and coherent (K-poor) endmembers. As shown by Caravaca et al. (this issue), the rubbly endmember is associated with finely laminated mudstones indicative of a quiet lacustrine environment, whereas the coherent endmember is associated with coarser-

grained and cross-stratified rocks indicative of a more dynamic environment (e.g., fluvial or lake margin). Therefore, their distinct compositions could be interpreted as an effect of sediment sorting, or as a change of sediment source. In the first hypothesis, clay minerals—including illite—would have been transported from outside the crater and preferentially concentrated in the finer particles, thus explaining the $K_2O$ enrichment of the finer-grained, rubbly bedrock. A problem with this interpretation is that the coherent bedrock would be expected to be the clay-poor component, but the XRD data show instead that it is clay-rich by Gale standards (Bristow et al., 2021; Thorpe et al., this issue). We cannot rule out the possibility that the rubbly bedrock may contain a higher amount of clay minerals than the coherent bedrock, but the CIA values—which are comparable for both endmembers (Figure 13)—suggest that this is not the case. In the second hypothesis, the rubbly bedrock would correspond to sediments originating from a distinct, illite-rich source region. Unfortunately, the lack of drill sample from the rubbly bedrock and the absence of orbital detection of illite in the watershed (Ehlmann & Buz, 2015) hinders our ability to fully evaluate the merit of these various scenarios.

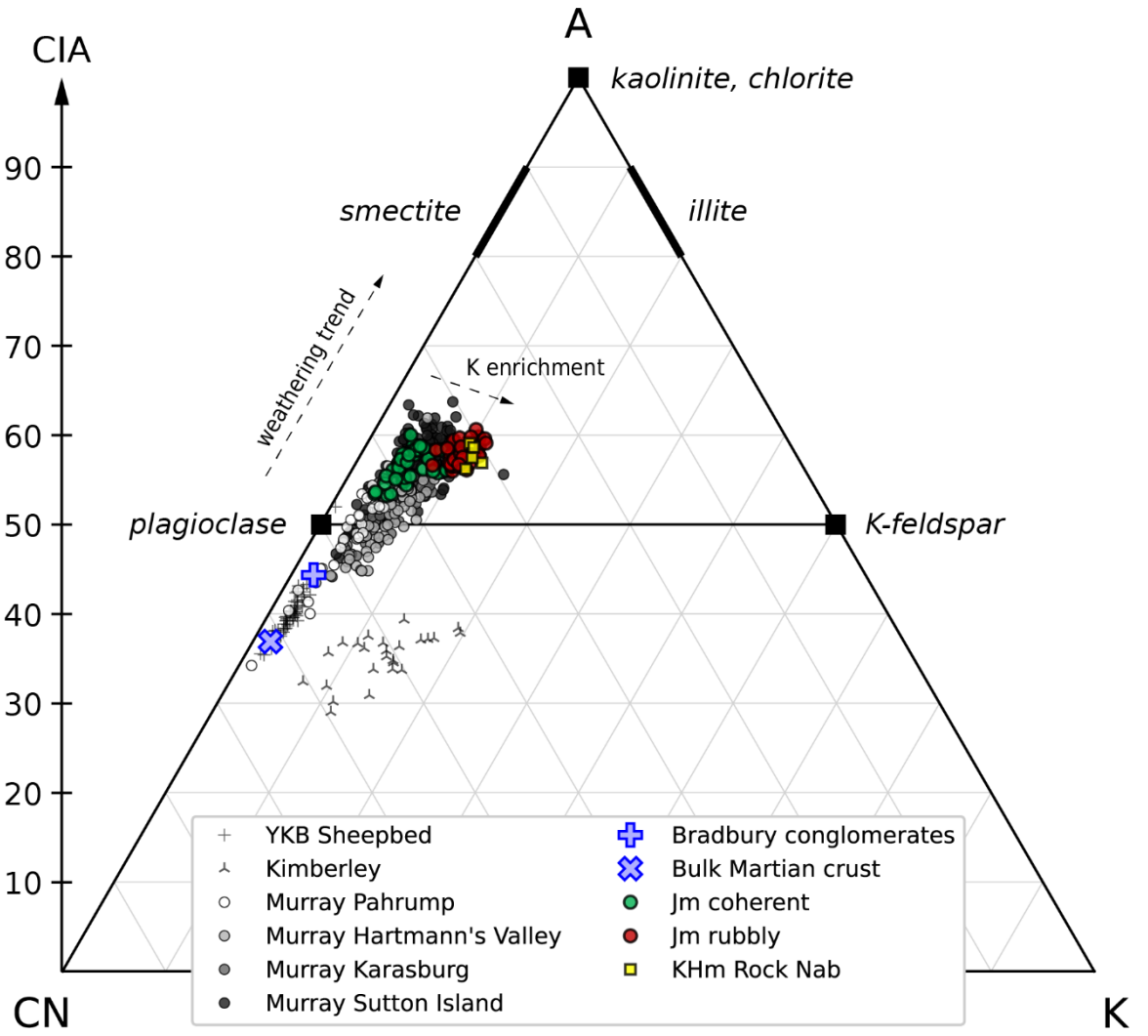


**Figure 12.** A-CN-K (A = $Al_2O_3$; CN = CaO+$Na_2O$; K = $K_2O$) ternary diagram comparing the Glen Torridon coherent and rubbly endmembers with other groups of targets from Gale crater. Each symbol corresponds to an individual bedrock target (average of at least 4 LIBS points; targets with fewer points are not shown). Data from previously visited stratigraphic units and

members are taken from Mangold et al. (2019) and displayed in grayscale. The mean composition of the Bradbury conglomerates (Mangold et al., 2016) and the estimated bulk composition of the Martian crust (Taylor & McLennan, 2009) are shown for reference. YKB = Yellowknife Bay.

### 4.5 Alteration history

#### 4.5.1 Baseline bedrock

The geochemical data acquired by ChemCam along *Curiosity*'s traverse in Glen Torridon shed light on the alteration history of the region. The bedrock displays elevated CIA values in all areas outside the Buttes (Figure 13), in line with other members of the Murray formation encountered earlier in the mission (Frydenvang et al., 2020; Mangold et al., 2019). These elevated values indicate that the bulk of the GT sediments underwent aqueous alteration at sufficiently high water-to-rock ratio to remove some of the mobile elements, particularly calcium, which is very low in targets from Types 1, 2 and 3 (Figure 9d). This episode of aqueous alteration is likely responsible for the formation of the majority of the clay minerals found in Glen Torridon. It probably occurred early in the history of the sediments, i.e., before, during, or shortly after their transport and deposition into Gale crater.

In addition to elevated CIA values, the Glen Torridon bedrock shows evidence for local remobilization of redox-sensitive elements. This is particularly the case in the Glasgow member, where Fe-rich dark-toned features were observed in several areas along the lateral traverse (Gasda et al., this issue). The bedrock in between the features is Fe-poor and Si-rich (Figure 5c-d), resulting in an overall negative correlation between $FeO_T$ and $SiO_2$ in the Glasgow member (Table S6). No other oxide quantified by ChemCam is significantly correlated with $FeO_T$, and no enhancement of the carbon signal is observed, suggesting that the dark-toned features are composed of a Fe-oxide phase, which in turn may explain the elevated hematite content detected by CheMin in the GG sample (Thorpe et al., this issue).

These observations are reminiscent of previous ones made on Vera Rubin ridge, where several types of dark-toned features were shown to be Fe-rich, and interpreted as crystalline hematite (L'Haridon et al., 2020). Some of them were surrounded by an Fe-poor "bleached" halo, indicating that the iron concentrated in the dark-toned features had mostly been remobilized from local rocks and not transported from elsewhere, in agreement with the absence of an overall enrichment in $FeO_T$ at the scale of the ridge (David et al., 2020; Frydenvang et al., 2020). Likewise, the average $FeO_T$ abundance of the baseline Glasgow bedrock is not higher than in the rest of Glen Torridon (Figure 9b). Based on the comparison with VRR, we infer that the dark-toned features of the Glasgow member also represent a small-scale remobilization of iron during diagenesis, possibly due to the circulation of reducing groundwater fluids (David et al., 2020; L'Haridon et al., 2020).

Additional indications of diagenetic remobilization of redox-sensitive elements were observed in the Mary Anning area. They consist of a Fe-rich bedrock layer (Figure 5a-b), and of Mn enrichments in both the bedrock and dark-toned nodules (Gasda et al., this issue). An attempt to sample these Mn-rich nodules was made at the Groken drill site (Lanza et al., 2021). Interestingly, other areas belonging to the Knockfarril Hill member do not display such evidence for remobilization of iron and manganese, which suggests a more localized process than in the Glasgow member.

#### 4.5.2 Hutton interval

The anomalous compositions measured near the top of Western Butte and in the Hutton interval (Type 4 defined in section 4.1) indicate that the sediments at these two

locations have undergone a distinct alteration history compared to the rest of Glen Torridon. The lower CIA values (Figure 13), which correlate with a lower amount of clay minerals detected by CheMin in the Hutton drill sample (Figure 10), may suggest that these sediments have simply been less strongly altered. However, this scenario (illustrated in Figure 14a) would require a significant shift in the alteration conditions and/or in the nature of the sediment source, even though these rocks appear to be the direct continuation of the Glasgow member from a sedimentological and stratigraphic point of view (Figure S1). In addition, the full mineralogy of the Hutton drill sample—which is characterized by the absence of olivine and the presence of significant amounts of cristobalite and opal-CT (Thorpe et al., this issue)—is distinct from the poorly altered materials analyzed elsewhere at Gale crater, such as the modern eolian deposits (Achilles et al., 2017; Bish et al., 2013) or the fossilized ones of the Stimson formation (Yen et al., 2017). Finally, the fact that Hutton-like compositions were not found again laterally when *Curiosity* drove toward to the "sulfate-bearing unit" (O'Connell-Cooper et al., this issue) argues against a general shift in sediment composition throughout the Glasgow member at the level of the Hutton interval.

Conversely, the location of the anomalous compositions suggests that their genesis may be related to the presence of the Siccar Point unconformity. Moreover, the fact that they coincide with the appearance of numerous diagenetic features embedded in the bedrock likely indicates that fluids were involved and circulated through the porosity of the sediments. Therefore, in this second scenario (illustrated in Figure 14b), the sediments forming the Glasgow member would have been initially homogeneous (with a composition close to that of the underlying members), and later modified by the circulation of fluids along the pediment surface, either before or after the deposition of the Stimson formation. However, instead of causing further leaching (which would have resulted in even higher CIA values), the fluids would have been already concentrated in mobile elements that may have subsequently precipitated in the porosity and caused the CIA values to decrease. From a geochemical standpoint, this scenario can be reproduced by a simple dilution model, in which a material composed of mobile and volatile elements—including Fe, Ca, Mg, Na, and F (see Text S3 and Table S7)—is added to a baseline Glasgow composition. Interestingly, such dilution model allows to explain the lower $SiO_2$ content of the Type 4 bedrock (Figure 9a) without removing any silica from the system—this is instead a passive decrease, due to the addition of other elements.

Nonetheless, this model would also require significant mineralogical reactions, because the mineralogy of the Hutton drill sample cannot be explained by a simple dilution of the Glasgow sample. Indeed, the latter contains ~24 wt% clay minerals, whereas the former contains only ~6 wt% (Thorpe et al., this issue); such a decrease would require a dilution factor much higher than modeled from the chemistry (Table S7). In addition, the presence of significant amounts of cristobalite and opal-CT in the Hutton sample despite the lower $SiO_2$ content of the Type 4 bedrock likely indicates the destruction of pre-existing silicate phases, including clay minerals. A similar process is suspected to have occurred in the rocks of Vera Rubin ridge, which show low abundances of clay minerals compared to adjacent terrains. Based on the identification of gray hematite in the Highfield sample, Rampe et al. (2020) proposed a model involving warm (100-200 °C) and/or acidic fluids. The detection of F-rich targets in the Hutton interval (Figure 7) could be another indication of the circulation of warm or acidic diagenetic fluids, as proposed for the Garden City outcrop of the Pahrump Hills member (Nachon et al., 2017). Alternatively, Bristow et al. (2021) argued that the percolation of silica-poor brines at low temperature (<50 °C) and neutral to slightly acidic pH could be the cause of the destruction of the VRR smectites. In their model, the fluids would have originated from the overlying "sulfate-bearing unit", and may have led to the deposition of

Mg-sulfates such as those identified by Rapin et al. (2019) in the Sutton Island member. Thus, this model could be transposed to Glen Torridon to explain the low abundance of clay minerals in the Hutton interval of the Glasgow member, but also the presence of Mg-sulfates that we interpret to be the reason of the MgO enrichment in the coherent bedrock of the Jura and Knockfarril Hill members (see section 4.3). Nonetheless, the model of Bristow et al. (2021) may not be directly applicable, because the Hutton interval has an anomalous chemical composition, whereas the VRR bedrock is overall geochemically similar to the adjacent members of the Murray formation (Frydenvang et al., 2020). In particular, the Hutton interval displays a low CIA value, whereas the VRR bedrock retained comparatively high CIA values despite their low abundance of clay minerals (Figure 10). These differences may be due to spatial and/or temporal variations of the compositions of the diagenetic fluids; for example, those that interacted with the Hutton interval may have been more concentrated, leading to supersaturation and precipitation of various compounds in the porosity of the sediments, as inferred from our dilution model (Table S7).

Finally, it is noteworthy that the anomalous bedrock appears to retain the negative correlation between $FeO_T$ and $SiO_2$ observed elsewhere in the Glasgow member (Tables S5 and S6), even though the Fe-rich dark-toned features themselves are only observed in the baseline Glasgow bedrock (i.e., away from the Buttes). This would be consistent with the hypothesis that the two types of bedrock were initially more similar to each other, as in our second scenario (Figure 14b). Furthermore, this would indicate that the diagenetic event that caused the remobilization of iron within the Glasgow bedrock occurred before the one that created the anomalous bedrock below the Siccar Point unconformity.

#### 4.5.3 Summary

Based on the above discussion, the alteration history of the Glen Torridon region appears to have involved at least four main aqueous events:

1. bulk, open-system alteration of the sediments (or their source rocks), resulting in the formation of the majority of the clay minerals identified by CheMin and detected by orbital instruments—this step may have accompanied or followed by low-grade burial diagenesis causing partial illitization of the smectites;
2. circulation of—possibly reducing—diagenetic fluids, causing the small-scale remobilization of redox-sensitive elements throughout the Glasgow member, and more locally within the Knockfarril Hill member;
3. after the formation of the Greenheugh pediment surface by erosion, circulation of concentrated diagenetic fluids, generating the anomalous bedrock observed today near the top of Western butte and in the Hutton interval;
4. after complete lithification of the sediments, circulation of late-stage fluids within the fractures and emplacement of the ubiquitous Ca-sulfate veins.

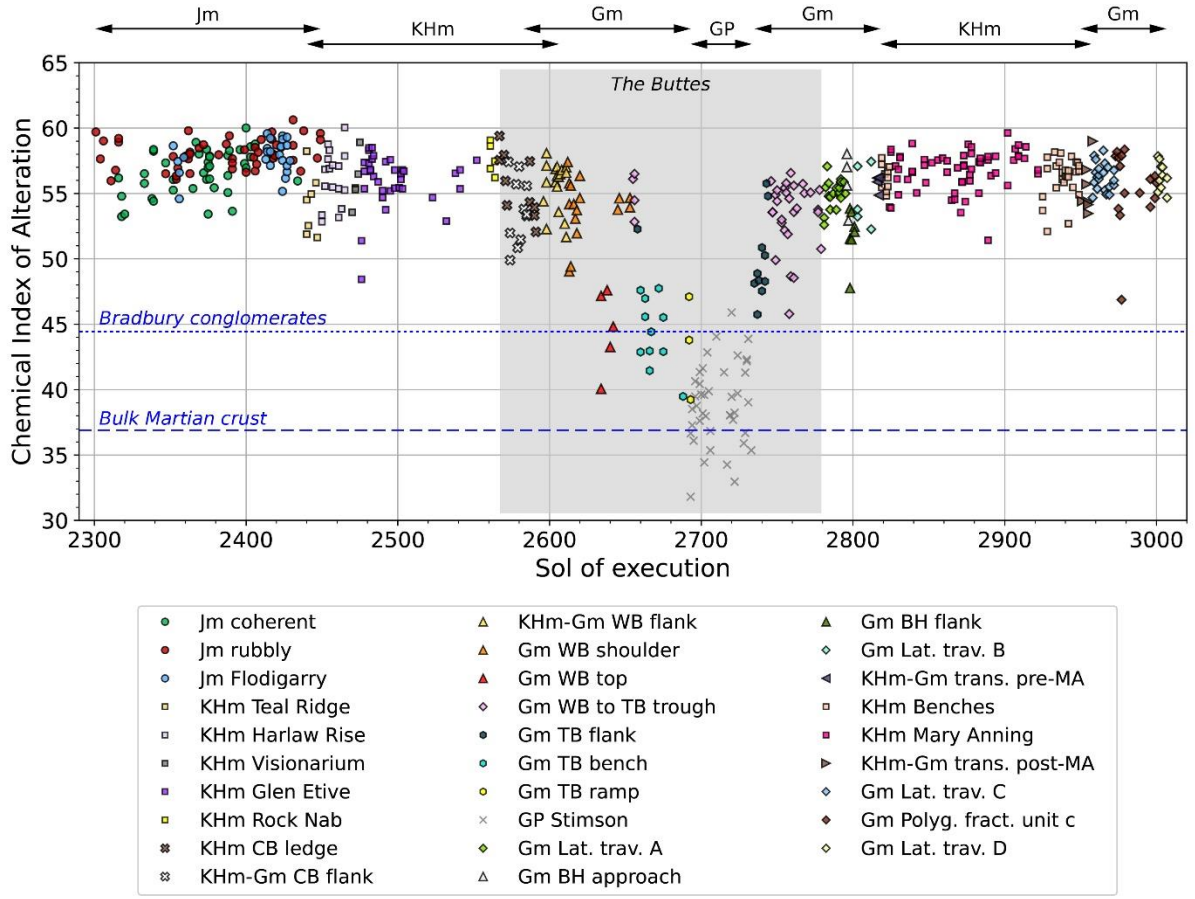


**Figure 13.** Variations of CIA values along *Curiosity*'s entire traverse across the Glen Torridon region. Each symbol corresponds to an individual bedrock target (average of at least 4 LIBS points; targets with less points are not shown). The x axis corresponds to time of measurement and does not reflect horizontal distance (see Figure 1 for localization). The Greenheugh pediment (GP) targets belong to the younger Stimson formation but are included for comparison. BH = Bloodstone hill; CB = Central butte; Gm = Glasgow member; Jm = Jura member; KHm = Knockfarril Hill member; Lat. trav. = lateral traverse; MA = Mary Anning; Polyg. fract. unit c = Polygonally fractured unit c (Hughes, 2021); TB = Tower butte; trans. = transition; WB = Western butte.

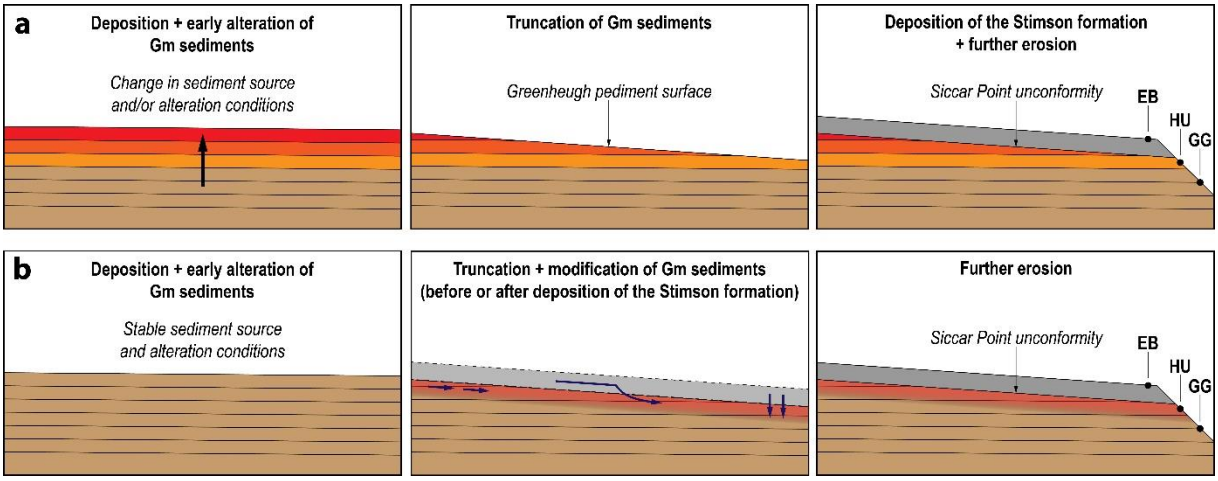


**Figure 14.** Two possible scenarios to explain the formation of the anomalous bedrock observed in the Glasgow member (Gm) just below the Siccar Point unconformity. Drill sample abbreviations: GG = Glasgow; HU = Hutton; EB = Edinburgh.

### 4.6 Implications for orbital observations

As mentioned in the introduction, the Glen Torridon region has been a primary target for the MSL team ever since *Curiosity*'s landing because of the clear signatures of clay minerals detected from orbit (Grotzinger et al., 2012; Milliken et al., 2010). More specifically, one objective of the campaign was to better understand why these signatures are more spatially extensive in Glen Torridon compared to previous terrains, even though clay minerals had already been detected in significant abundances at several locations along the traverse (Bristow et al., 2018; Rampe et al., 2017; Vaniman et al., 2014). The two main hypotheses were: (1) that the bedrock in Glen Torridon is significantly more altered and contains a much higher abundance of clay minerals than the terrains explored earlier in the mission; or (2) that the detectability of clay minerals is enhanced in Glen Torridon by extrinsic factors—i.e., not related to the composition of the rocks themselves (Fox et al., 2020; Bennett et al., this issue).

In this paper, we have shown that the CIA values measured by ChemCam in Glen Torridon are elevated by Martian standards (Figures 12 and 13), suggesting that the clay minerals detected from orbit have been formed through open-system weathering. However, similarly high CIA values have been observed in other members of the Murray formation visited previously (Frydenvang et al., 2020; Mangold et al., 2019). In parallel, the XRD analyses performed by the CheMin instrument have shown that the Glen Torridon samples (excluding Hutton) are some of the most clay-rich of the entire traverse, with abundances ranging from ~24 to ~34 wt% (Thorpe et al., this issue). However, these values are only marginally higher than for the Marimba drill sample from the Karasburg member, which contained ~28 wt% clay minerals (Figure 10; Bristow et al., 2018). Thus, overall, the Glen Torridon region does not show significantly increased aqueous alteration compared to some other parts of the Murray formation, which in turn implies that some extrinsic factors contribute to the enhanced detectability of the clay minerals from orbit. This situation is somewhat analogous to what is observed at Vera Rubin ridge, where stronger signatures of hematite are detected from orbit, but are not correlated with significant hematite or iron enrichments in the bedrock, implying that other factors are at play (Fraeman et al., 2020; Frydenvang et al., 2020; Rampe et al., 2020).

In Glen Torridon, these factors may include a reduction in dust or sand cover: for example, the Vera Rubin ridge may act as a physical barrier against the sand particles coming

from the Bagnold dune field to the north, although other bodies of sand do occur within Glen Torridon (e.g., the "Sands of Forvie"; Figure 1). It is also possible that the distinctive outcrop expression of the rubbly bedrock—which is the spatially dominant component of the Jura member, where the clay signatures are the strongest—may increase the interaction of the incident light with the minerals, thus enhancing the absorption features. A detailed investigation of these possible factors is deferred to a future study, but would likely be highly beneficial for our understanding of the orbital detections of secondary minerals on Mars and other planets.

## 5 Conclusion

The exploration of Glen Torridon by the *Curiosity* rover has allowed the MSL team to investigate the geologic setting of what was known until then as the "clay-bearing unit" of Gale crater. In particular, the data collected by the ChemCam instrument reveal the details of the bedrock geochemistry and shed light into the alteration history of the region. Our results show that, in the Jura member, the spatially dominant component—which is the main contributor to the spectral signatures observed from orbit, but was unfortunately not sampled by the drill due its rubbly nature—has a remarkably homogeneous composition and is enriched in both $K_2O$ and $SiO_2$. These enrichments are best explained by the presence of illite (or more likely a mixed-layer illite/smectite phase), as opposed to K-feldspars. The coherent bedrock of the Jura and Knockfarril Hill members has a composition somewhat variable from one location to another, but is overall enriched in MgO, which may be due to small amounts of Mg-sulfates. The Glasgow member shows a stronger diagenetic overprint, especially near the top of Western butte and in the Hutton interval, where the bedrock composition deviates significantly from the rest of Glen Torridon and probably records the circulation of concentrated fluids late in the history of Gale (i.e., after the formation of the Greenheugh pediment surface). Nonetheless, the bulk of the aqueous alteration of the Glen Torridon sediments occurred early, possibly before or during their transport into the crater, and likely involved dilute meteoric fluids at low temperature and relatively high water-to-rock ratio. Finally, the CIA values measured by ChemCam and the amounts of clay minerals found by the CheMin XRD instrument suggest that Glen Torridon did not experience a significantly greater degree of aqueous alteration than some other members of the Murray formation visited previously by *Curiosity*, which in turn implies that non-compositional factors such as dust/sand cover and/or the particular outcrop expression of the rubbly bedrock are the cause of the enhanced spectral signatures of clay minerals seen from orbit.

## Acknowledgments

The authors warmly thank the MSL and ChemCam operations teams for the collection of the data used in this paper, especially in the context of the COVID-19 pandemic. The authors also thank the entire MSL science team for insightful discussions throughout the Glen Torridon campaign, and the "sed-strat" group (especially Chris Fedo, Lauren Edgar and John Grotzinger) for producing the stratigraphic column of the region and mapping the member boundaries. Mastcam mosaics were processed by the Mastcam team at Malin Space Science Systems. The authors thank Gilles Berger for discussions about illitization, as well as two anonymous reviewers for their constructive comments that helped improve the manuscript. This work was supported by the Centre National d'Études Spatiales (CNES). NM and GC acknowledge support from the Agence Nationale de la Recherche (ANR) under the contract ANR-16-CE31-0012 entitled "Mars-Prime". JF acknowledges support from the Carlsberg Foundation. Any use of trade, firm, or product names is for descriptive purposes only and does not imply endorsement by the U.S. Government.

## Open Research

Data availability statement: All ChemCam LIBS spectra and derived major-element oxide compositions used in this paper are available through the NASA Planetary Data System (Wiens, 2013). In addition, the point-by-point classification used to group, analyze and interpret the data is provided in Table S1, and also available online (Dehouck, 2022).

## References


Achilles, C. N., Downs, R. T., Ming, D. W., Rampe, E. B., Morris, R. V., Treiman, A. H., et al. (2017). Mineralogy of an active eolian sediment from the Namib dune, Gale crater, Mars. *Journal of Geophysical Research: Planets*, *122*(11), 2344–2361. https://doi.org/10.1002/2017JE005262

Ajouyed, O., Hurel, C., & Marmier, N. (2011). Evaluation of the Adsorption of Hexavalent Chromium on Kaolinite and Illite. *Journal of Environmental Protection*, *02*(10), 1347. https://doi.org/10.4236/jep.2011.210155

Bedford, C. C., Banham, S., Bridges, J. C., Forni, O., Cousin, A., Bowden, B., et al. (this issue). An insight into ancient aeolian processes and post-Noachian aqueous alteration in Gale crater, Mars, using ChemCam geochemical data from the Greenheugh capping unit. *Journal of Geophysical Research: Planets*

Bennett, K. A., Fox, V. K., Bryk, A., Dietrich, W., Fedo, C., Edgar, L., et al. (this issue). An Overview of the Curiosity Rover's Campaign in Glen Torridon, Gale Crater, Mars. *Journal of Geophysical Research: Planets*

Bibring, J. P., Langevin, Y., Mustard, J. F., Poulet, F., Arvidson, R., Gendrin, A., et al. (2006). Global mineralogical and aqueous Mars history derived from OMEGA/Mars express data. *Science*, *312*(5772), 400–404. https://doi.org/10.1126/science.1122659

Bish, D. L., Blake, D. F., Vaniman, D. T., Chipera, S. J., Morris, R. V., Ming, D. W., et al. (2013). X-ray Diffraction Results from Mars Science Laboratory: Mineralogy of Rocknest at Gale Crater. *Science*, *341*(6153). https://doi.org/10.1126/science.1238932

Blake, D. F., Vaniman, D. T., Achilles, C. N., Anderson, R., Bish, D. L., Bristow, T. F., et al. (2012), Characterization and calibration of the CheMin mineralogical instrument on Mars Science Laboratory, *Space Science Reviews*, *170*(1-4), 341–399. https://doi.org/10.1007/s11214-012-9912-2

Blaney, D. L., Wiens, R. C., Maurice, S., Clegg, S. M., Anderson, R. B., Kah, L. C., et al. (2014). Chemistry and texture of the rocks at Rocknest, Gale Crater: Evidence for sedimentary origin and diagenetic alteration. *Journal of Geophysical Research: Planets*, *119*(9), 2013JE004590. https://doi.org/10.1002/2013JE004590

Borlina, C. S., Ehlmann, B. L., & Kite, E. S. (2015). Modeling the thermal and physical evolution of Mount Sharp's sedimentary rocks, Gale Crater, Mars: Implications for diagenesis on the MSL Curiosity rover traverse. *Journal of Geophysical Research: Planets*, *120*(8), 2015JE004799. https://doi.org/10.1002/2015JE004799

Bristow, T. F., Grotzinger, J. P., Rampe, E. B., Cuadros, J., Chipera, S. J., Downs, G. W., et al. (2021). Brine-driven destruction of clay minerals in Gale crater, Mars. *Science*, *373*(6551), 198–204. https://doi.org/10.1126/science.abg5449

Bristow, Thomas F., Rampe, E. B., Achilles, C. N., Blake, D. F., Chipera, S. J., Craig, P., et al. (2018). Clay mineral diversity and abundance in sedimentary rocks of Gale crater, Mars. *Science Advances*, *4*(6), eaar3330. https://doi.org/10.1126/sciadv.aar3330

Caravaca, G., Mangold, N., Dehouck, E., Schieber, J., Zaugg, L., Bryk, A. B., et al. (this issue). From Lake to River: Documenting an Environmental Transition across the Jura/Knockfarril Hill Members Boundary in the Glen Torridon Region of Gale crater (Mars). *Journal of Geophysical Research: Planets*

Carter, J., Poulet, F., Bibring, J. P., Mangold, N., & Murchie, S. (2013). Hydrous minerals on Mars as seen by the CRISM and OMEGA imaging spectrometers: Updated global view. *Journal of Geophysical Research: Planets*, 1–29.

Clegg, S. M., Wiens, R. C., Anderson, R. B., Forni, O., Frydenvang, J., Lasue, J., et al. (2017). Recalibration of the Mars Science Laboratory ChemCam instrument with an expanded geochemical database. *Spectrochimica Acta Part B: Atomic Spectroscopy*, *129*, 64–85. https://doi.org/10.1016/j.sab.2016.12.003

Cousin, A., Sautter, V., Payré, V., Forni, O., Mangold, N., Gasnault, O., et al. (2017a). Classification of igneous rocks analyzed by ChemCam at Gale crater, Mars. *Icarus*, *288*, 265–283. https://doi.org/10.1016/j.icarus.2017.01.014

Cousin, A., Dehouck, E., Meslin, P.-Y., Forni, O., Williams, A. J., Stein, N., et al. (2017b). Geochemistry of the Bagnold dune field as observed by ChemCam and comparison with other aeolian deposits at Gale Crater. *Journal of Geophysical Research: Planets*, *122*(10), 2144–2162. https://doi.org/10.1002/2017JE005261

David, G., Cousin, A., Forni, O., Meslin, P.-Y., Dehouck, E., Mangold, N., et al. (2020). Analyses of High-Iron Sedimentary Bedrock and Diagenetic Features Observed With ChemCam at Vera Rubin Ridge, Gale Crater, Mars: Calibration and Characterization. *Journal of Geophysical Research: Planets*, *125*(10), e2019JE006314. https://doi.org/10.1029/2019JE006314

Dehouck, E. (2022). Classification of ChemCam LIBS targets from Glen Torridon, Gale crater, Mars [Data set]. *Zenodo*. https://doi.org/10.5281/zenodo.5902566

Edgar, L. A., Fedo, C. M., Gupta, S., Banham, S. G., Fraeman, A. A., Grotzinger, J. P., et al. (2020). A Lacustrine Paleoenvironment Recorded at Vera Rubin Ridge, Gale Crater: Overview of the Sedimentology and Stratigraphy Observed by the Mars ScienceLaboratory Curiosity Rover. *Journal of Geophysical Research: Planets*, *125*(3), e2019JE006307. https://doi.org/10.1029/2019JE006307

Edgett, K. S., Yingst, R. A., Ravine, M. A., Caplinger, M. A., Maki, J. N., Ghaemi, F. T., et al. (2012). Curiosity's Mars Hand Lens Imager (MAHLI) Investigation. *Space Science Reviews*, *170*(1), 259–317. https://doi.org/10.1007/s11214-012-9910-4

Ehlmann, B. L., & Buz, J. (2015). Mineralogy and fluvial history of the watersheds of Gale, Knobel, and Sharp craters: A regional context for the Mars Science Laboratory Curiosity's exploration. *Geophysical Research Letters*, *42*(2), 264–273. https://doi.org/10.1002/2014GL062553

Fedo, C. M., Grotzinger, J. P., Bryk, A., Edgar, L. A., Bennett, K., Fox, V., et al. (2020). Ground-based stratigraphic correlation of the Jura and Knockfarril Hill members of the Murray formation, Gale crater: Bridging the Vera Rubin ridge – Glen Torridon divide, Lunar and Planetary Science Conference, Abstract #2345, *Lunar Planet. Inst.*, Houston, Texas

Forni, O., Gaft, M., Toplis, M. J., Clegg, S. M., Maurice, S., Wiens, R. C., et al. (2015). First detection of fluorine on Mars: Implications for Gale Crater's geochemistry. *Geophysical Research Letters*, *42*(4), 1020–1028. https://doi.org/10.1002/2014GL062742

Fraeman, A. A., Ehlmann, B. L., Arvidson, R. E., Edwards, C. S., Grotzinger, J. P., Milliken, R. E., et al. (2016). The stratigraphy and evolution of lower Mount Sharp from spectral, morphological, and thermophysical orbital data sets. *Journal of Geophysical Research: Planets*, *121*(9), 1713–1736. https://doi.org/10.1002/2016JE005095

Fraeman, A. A., Edgar, L. A., Rampe, E. B., Thompson, L. M., Frydenvang, J., Fedo, C. M., et al. (2020). Evidence for a Diagenetic Origin of Vera Rubin Ridge, Gale Crater, Mars: Summary and Synthesis of Curiosity's Exploration Campaign. *Journal of Geophysical Research: Planets*, *125*(12), e2020JE006527. https://doi.org/10.1029/2020JE006527

Frydenvang, J., Mangold, N., Wiens, R. C., Fraeman, A. A., Edgar, L. A., Fedo, C. M., et al. (2020). The Chemostratigraphy of the Murray Formation and Role of Diagenesis at Vera Rubin Ridge in Gale Crater, Mars, as Observed by the ChemCam Instrument. *Journal of Geophysical Research: Planets*, *125*(9), e2019JE006320. https://doi.org/10.1029/2019JE006320

Fox, V. K., Bennett, K., Bryk, A., & Arvidson, R. E. (2020). One Year in Glen Torridon: Key Results from the Mars Science Laboratory Curiosity Rover exploration of clay-bearing units, Lunar and Planetary Science Conference, Abstract #2833, *Lunar Planet. Inst.*, Houston, Texas

Gasda, P. J., Haldeman, E. B., Wiens, R. C., Rapin, W., Bristow, T. F., Bridges, J. C., et al. (2017). In situ detection of boron by ChemCam on Mars. *Geophysical Research Letters*, *44*(17), 8739–8748. https://doi.org/10.1002/2017GL074480

Gasda, P. J., Anderson, R. B., Cousin, A., Forni, O., Clegg, S. M., Ollila, A., et al. (2021). Quantification of manganese for ChemCam Mars and laboratory spectra using a multivariate model. *Spectrochimica Acta Part B: Atomic Spectroscopy*, *181*, 106223. https://doi.org/10.1016/j.sab.2021.106223

Gasda, P. J., Comellas, J., Essunfeld, A., Das, D., Bryk, A. B., Dehouck, E., et al. (this issue). Overview of the Morphology and Chemistry of Diagenetic Features in the Clay-Rich Glen Torridon Unit of Gale Crater, Mars. *Journal of Geophysical Research: Planets*

Goetz, W., Dehouck, E., Gasda, P., Johnson, J., Meslin, P.-Y., Lanza, N., et al. (this issue). Detection of copper by the ChemCam instrument along Curiosity's traverse in Gale crater, Mars: Elevated abundances in Glen Torridon. *Journal of Geophysical Research: Planets*

Grotzinger, J. P., Crisp, J., Vasavada, A. R., Anderson, R. C., Baker, C. J., Barry, R., et al. (2012). Mars Science Laboratory Mission and Science Investigation. *Space Science Reviews*, *170*(1), 5–56. https://doi.org/10.1007/s11214-012-9892-2

Grotzinger, J. P., Sumner, D. Y., Kah, L. C., Stack, K., Gupta, S., Edgar, L., et al. (2014). A Habitable Fluvio-Lacustrine Environment at Yellowknife Bay, Gale Crater, Mars. *Science*, *343*(6169). https://doi.org/10.1126/science.1242777

Grotzinger, J. P., Gupta, S., Malin, M. C., Rubin, D. M., Schieber, J., Siebach, K., et al. (2015). Deposition, exhumation, and paleoclimate of an ancient lake deposit, Gale crater, Mars. *Science*, *350*(6257). https://doi.org/10.1126/science.aac7575

Hughes, M. N. (2021). Landscape Evolution at Endeavour and Gale Craters on Mars, and How Terrain Characteristics Correlate with Mineralogy on Lower Mount Sharp, Gale Crater. *Arts & Sciences Electronic Theses and Dissertations*, 2428. https://doi.org/10.7936/c6se-5895

Hurowitz, J. A., Grotzinger, J. P., Fischer, W. W., McLennan, S. M., Milliken, R. E., Stein, N., et al. (2017). Redox stratification of an ancient lake in Gale crater, Mars. *Science*, *356*(6341), eaah6849. https://doi.org/10.1126/science.aah6849

Kronyak, R. E., Kah, L. C., Edgett, K. S., VanBommel, S. J., Thompson, L. M., Wiens, R. C., et al. (2019). Mineral-Filled Fractures as Indicators of Multigenerational Fluid Flow in the Pahrump Hills Member of the Murray Formation, Gale Crater, Mars. *Earth and Space Science*, *6*(2), 238–265. https://doi.org/10.1029/2018EA000482

Lanza, N. L., Gasda, P. J., Essunfeld, A., Comellas, J., Caravaca, G., Rampe, E., et al. (2021). Chemistry of Manganese-Bearing Materials at the Groken Drill Site, Gale Crater, Mars. Lunar and Planetary Science Conference, Abstract #2231, *Lunar Planet. Inst.*, Houston, Texas

Lasue, J., Clegg, S. M., Forni, O., Cousin, A., Wiens, R. C., Lanza, N., et al. (2016). Observation of > 5 wt % zinc at the Kimberley outcrop, Gale crater, Mars. *Journal of Geophysical Research: Planets*, *121*(3), 338–352. https://doi.org/10.1002/2015JE004946

Lasue, J., Cousin, A., Meslin, P.-Y., Mangold, N., Wiens, R. C., Berger, G., et al. (2018). Martian Eolian Dust Probed by ChemCam. *Geophysical Research Letters*, *45*(20), 10,968-10,977. https://doi.org/10.1029/2018GL079210

Le Deit, L., Hauber, E., Fueten, F., Pondrelli, M., Rossi, A. P., & Jaumann, R. (2013). Sequence of infilling events in Gale Crater, Mars: Results from morphology, stratigraphy, and mineralogy. *Journal of Geophysical Research: Planets*, *118*(12), 2012JE004322. https://doi.org/10.1002/2012JE004322

Le Deit, L., Mangold, N., Forni, O., Cousin, A., Lasue, J., Schröder, S., et al. (2016). The potassic sedimentary rocks in Gale Crater, Mars, as seen by ChemCam on board Curiosity. *Journal of Geophysical Research: Planets*, *121*(5), 2015JE004987. https://doi.org/10.1002/2015JE004987

Le Mouélic, S., Gasnault, O., Herkenhoff, K. E., Bridges, N. T., Langevin, Y., Mangold, N., et al. (2015). The ChemCam Remote Micro-Imager at Gale crater: Review of the first year of operations on Mars. *Icarus*, *249*, 93–107. https://doi.org/10.1016/j.icarus.2014.05.030

L'Haridon, J., Mangold, N., Meslin, P.-Y., Johnson, J. R., Rapin, W., Forni, O., et al. (2018). Chemical variability in mineralized veins observed by ChemCam on the lower slopes of Mount Sharp in Gale crater, Mars. *Icarus*, *311*, 69–86. https://doi.org/10.1016/j.icarus.2018.01.028

L'Haridon, J., Mangold, N., Fraeman, A. A., Johnson, J. R., Cousin, A., Rapin, W., et al. (2020). Iron Mobility During Diagenesis at Vera Rubin Ridge, Gale Crater, Mars. *Journal of Geophysical Research: Planets*, *125*(11), e2019JE006299. https://doi.org/10.1029/2019JE006299

Mahaffy, P. R., Webster, C. R., Cabane, M., Conrad, P. G., Coll, P., Atreya, S. K., et al. (2012). The Sample Analysis at Mars Investigation and Instrument Suite. *Space Science Reviews*, *170*(1), 401–478. https://doi.org/10.1007/s11214-012-9879-z

Maki, J., Thiessen, D., Pourangi, A., Kobzeff, P., Litwin, T., Scherr, L., et al. (2012). The Mars Science Laboratory Engineering Cameras. *Space Science Reviews*, *170*(1), 77–93. https://doi.org/10.1007/s11214-012-9882-4

Malin, M. C., Ravine, M. A., Caplinger, M. A., Ghaemi, F. T., Schaffner, J. A., Maki, J. N., et al. (2017). The Mars Science Laboratory (MSL) Mast cameras and Descent imager: Investigation and instrument descriptions. *Earth and Space Science*, *4*(8), 506–539. https://doi.org/10.1002/2016EA000252

Mangold, N., Forni, O., Dromart, G., Stack, K., Wiens, R. C., Gasnault, O., et al. (2015). Chemical variations in Yellowknife Bay formation sedimentary rocks analyzed by ChemCam on board the Curiosity rover on Mars. *Journal of Geophysical Research: Planets*, *120*(3), 2014JE004681. https://doi.org/10.1002/2014JE004681

Mangold, N., Thompson, L. M., Forni, O., Williams, A. J., Fabre, C., Deit, L. L., et al. (2016). Composition of conglomerates analyzed by the Curiosity rover: Implications for Gale Crater crust and sediment sources. *Journal of Geophysical Research: Planets*, *121*(3), 353–387. https://doi.org/10.1002/2015JE004977

Mangold, N., Dehouck, E., Fedo, C., Forni, O., Achilles, C., Bristow, T., et al. (2019). Chemical alteration of fine-grained sedimentary rocks at Gale crater. *Icarus*, *321*, 619–631. https://doi.org/10.1016/j.icarus.2018.11.004

Maurice, S., Wiens, R. C., Saccoccio, M., Barraclough, B., Gasnault, O., Forni, O., et al. (2012). The ChemCam Instrument Suite on the Mars Science Laboratory (MSL) Rover: Science Objectives and Mast Unit Description. *Space Science Reviews*, *170*(1–4), 95–166. https://doi.org/10.1007/s11214-012-9912-2

Maurice, S., Clegg, S. M., Wiens, R. C., Gasnault, O., Rapin, W., Forni, O., et al. (2016). ChemCam activities and discoveries during the nominal mission of the Mars Science Laboratory in Gale crater, Mars. *Journal of Analytical Atomic Spectrometry*, *31*(4), 863–889. https://doi.org/10.1039/C5JA00417A

McLennan, S. M., Anderson, R. B., Bell, J. F., III, Bridges, J. C., Calef, F., III, Campbell, J. L., et al. (2014). Elemental Geochemistry of Sedimentary Rocks at Yellowknife Bay, Gale Crater, Mars. *Science*, *343*(6169). https://doi.org/10.1126/science.1244734

Milliken, R. E., Grotzinger, J. P., & Thomson, B. J. (2010). Paleoclimate of Mars as captured by the stratigraphic record in Gale Crater. *Geophysical Research Letters*, *37*, L04201. https://doi.org/10.1029/2009gl041870

Nachon, M., Clegg, S. M., Mangold, N., Schröder, S., Kah, L. C., Dromart, G., et al. (2014). Calcium sulfate veins characterized by ChemCam/Curiosity at Gale crater, Mars. *Journal of Geophysical Research: Planets*, *119*(9), 2013JE004588. https://doi.org/10.1002/2013JE004588

Nachon, M., Mangold, N., Forni, O., Kah, L. C., Cousin, A., Wiens, R. C., et al. (2017). Chemistry of diagenetic features analyzed by ChemCam at Pahrump Hills, Gale crater, Mars. *Icarus*, *281*, 121–136. https://doi.org/10.1016/j.icarus.2016.08.026

Nesbitt, H. W., & Young, G. M. (1982). Early Proterozoic climates and plate motions inferred from major element chemistry of lutites. *Nature*, *299*(5885), 715–717. https://doi.org/10.1038/299715a0

O'Connell-Cooper, C. D., et al. (this issue). Geochemistry of the clay-bearing Glen Torridon region of Gale crater, Mars – APXS analysis of the Jura, Knockfarril Hill and Glasgow members. *Journal of Geophysical Research: Planets*

Payré, V., Fabre, C., Cousin, A., Sautter, V., Wiens, R. C., Forni, O., et al. (2017). Alkali trace elements in Gale crater, Mars, with ChemCam: Calibration update and geological

implications. *Journal of Geophysical Research: Planets*, *122*(3), 650–679. https://doi.org/10.1002/2016JE005201

Payré, V., Fabre, C., Sautter, V., Cousin, A., Mangold, N., Le Deit, L., et al. (2019). Copper enrichments in the Kimberley formation in Gale crater, Mars: Evidence for a Cu deposit at the source. *Icarus*, *321*, 736–751. https://doi.org/10.1016/j.icarus.2018.12.015

Peret, L., Gasnault, O., Dingler, R., Langevin, Y., Bender, S., Blaney, D., et al. (2016) Restoration of the autofocus capability of the ChemCam instrument onboard the Curiosity rover. 14th International Conference on Space Operations, Paper #2539, *American Institute of Aeronautics and Astronautics*. https://doi.org/10.2514/6.2016-2539

Pollastro, R. M. (1993). Considerations and applications of the illite/smectite geothermometer in hydrocarbon-bearing rocks of Miocene to Mississippian age. *Clays and Clay Minerals*, *41*(2), 119–133.

Rampe, E. B., Ming, D. W., Blake, D. F., Bristow, T. F., Chipera, S. J., Grotzinger, J. P., et al. (2017). Mineralogy of an ancient lacustrine mudstone succession from the Murray formation, Gale crater, Mars. *Earth and Planetary Science Letters*, *471*, 172–185. https://doi.org/10.1016/j.epsl.2017.04.021

Rampe, E. B., Bristow, T. F., Morris, R. V., Morrison, S. M., Achilles, C. N., Ming, D. W., et al. (2020). Mineralogy of Vera Rubin Ridge From the Mars Science Laboratory CheMin Instrument. *Journal of Geophysical Research: Planets*, *125*(9), e2019JE006306. https://doi.org/10.1029/2019JE006306

Rapin, W., Meslin, P.-Y., Maurice, S., Vaniman, D., Nachon, M., Mangold, N., et al. (2016). Hydration state of calcium sulfates in Gale crater, Mars: Identification of bassanite veins. *Earth and Planetary Science Letters*, *452*, 197–205. https://doi.org/10.1016/j.epsl.2016.07.045

Rapin, W., Ehlmann, B. L., Dromart, G., Schieber, J., Thomas, N. H., Fischer, W. W., et al. (2019). An interval of high salinity in ancient Gale crater lake on Mars. *Nature Geoscience*, 1–7. https://doi.org/10.1038/s41561-019-0458-8

Rosenberg, P. E. (2002). The nature, formation, and stability of end-member illite: A hypothesis. *American Mineralogist*, *87*(1), 103–107. https://doi.org/10.2138/am-2002-0111

Sautter, V., Toplis, M. J., Wiens, R. C., Cousin, A., Fabre, C., Gasnault, O., et al. (2015). In situ evidence for continental crust on early Mars. *Nature Geoscience*, *8*(8), 605–609. https://doi.org/10.1038/ngeo2474

Schmidt, M. E., Perrett, G. M., Bray, S. L., Bradley, N. J., Lee, R. E., Berger, J. A., et al. (2018). Dusty Rocks in Gale Crater: Assessing Areal Coverage and Separating Dust and Rock Contributions in APXS Analyses. *Journal of Geophysical Research: Planets*. https://doi.org/10.1029/2018JE005553

Schröder, S., Meslin, P.-Y., Gasnault, O., Maurice, S., Cousin, A., Wiens, R. C., et al. (2015). Hydrogen detection with ChemCam at Gale crater. *Icarus*, *249*, 43–61. https://doi.org/10.1016/j.icarus.2014.08.029

Stein, N., Grotzinger, J. P., Schieber, J., Mangold, N., Hallet, B., Newsom, H., et al. (2018). Desiccation cracks provide evidence of lake drying on Mars, Sutton Island member,

Murray formation, Gale Crater. *Geology*, *46*(6), 515–518. https://doi.org/10.1130/G40005.1

Summons, R. E., Amend, J. P., Bish, D., Buick, R., Cody, G. D., Des Marais, D. J., et al. (2011). Preservation of Martian Organic and Environmental Records: Final Report of the Mars Biosignature Working Group. *Astrobiology*, *11*(2), 157–181. https://doi.org/10.1089/ast.2010.0506

Taylor, S. R., & McLennan, S. (2009). *Planetary Crusts: Their Composition, Origin and Evolution*. Cambridge University Press.

Thomson, B. J., Bridges, N. T., Milliken, R., Baldridge, A., Hook, S. J., Crowley, J. K., et al. (2011). Constraints on the origin and evolution of the layered mound in Gale Crater, Mars using Mars Reconnaissance Orbiter data. *Icarus*, *214*(2), 413–432. https://doi.org/10.1016/j.icarus.2011.05.002

Thorpe, M. T., Bristow, T. F., Rampe, E. B., Tosca, N., Grotzinger, J. P., Bennett, K. A., et al. (this issue). Mars Science Laboratory CheMin data from the Glen Torridon region and the significance of lake-groundwater interactions in interpreting mineralogy and sedimentary history. *Journal of Geophysical Research: Planets*

Treiman, A. H., Bish, D. L., Vaniman, D. T., Chipera, S. J., Blake, D. F., Ming, D. W., et al. (2016). Mineralogy, provenance, and diagenesis of a potassic basaltic sandstone on Mars: CheMin X-ray diffraction of the Windjana sample (Kimberley area, Gale Crater). *Journal of Geophysical Research: Planets*, *121*(1), 2015JE004932. https://doi.org/10.1002/2015JE004932

Vaniman, D. T., Bish, D. L., Ming, D. W., Bristow, T. F., Morris, R. V., Blake, D. F., et al. (2014). Mineralogy of a Mudstone at Yellowknife Bay, Gale Crater, Mars. *Science*, *343*(6169). https://doi.org/10.1126/science.1243480

Vaniman, David T., & Chipera, S. J. (2006). Transformations of Mg- and Ca-sulfate hydrates in Mars regolith. *American Mineralogist*, *91*(10), 1628–1642. https://doi.org/10.2138/am.2006.2092

Vaniman, David T., Martínez, G. M., Rampe, E. B., Bristow, T. F., Blake, D. F., Yen, A. S., et al. (2018). Gypsum, bassanite, and anhydrite at Gale crater, Mars. *American Mineralogist*, *103*(7), 1011–1020. https://doi.org/10.2138/am-2018-6346

Velde, B., & Vasseur, G. (1992). Estimation of the diagenetic smectite to illite transformation in time-temperature space. *American Mineralogist*, *77*(9–10), 967–976.

Wiens, R. C. (2013). MSL ChemCam Laser Induced Breakdown Spectrometer derived data, MSL-M-CHEMCAM-LIBS-5-RDR-V1.0 [Data set]. *NASA Planetary Data System*. https://doi.org/10.17189/1519485

Wiens, R. C., Maurice, S., Barraclough, B., Saccoccio, M., Barkley, W. C., Bell, J. F., III, et al. (2012). The ChemCam Instrument Suite on the Mars Science Laboratory (MSL) Rover: Body Unit and Combined System Tests. *Space Science Reviews*, *170*(1–4), 167–227. https://doi.org/10.1007/s11214-012-9902-4

Wiens, R. C., Maurice, S., Lasue, J., Forni, O., Anderson, R. B., Clegg, S., et al. (2013). Pre-flight calibration and initial data processing for the ChemCam laser-induced breakdown spectroscopy instrument on the Mars Science Laboratory rover. *Spectrochimica Acta Part B: Atomic Spectroscopy*, *82*, 1–27. https://doi.org/10.1016/j.sab.2013.02.003

Wiens, R. C., Blazon-Brown, A. J., Melikechi, N., Frydenvang, J., Dehouck, E., Clegg, S. M., et al. (2021). Improving ChemCam LIBS long-distance elemental compositions using empirical abundance trends. *Spectrochimica Acta Part B: Atomic Spectroscopy*, *182*, 106247. https://doi.org/10.1016/j.sab.2021.106247

Williams, L. B., & Hervig, R. L. (2005). Lithium and boron isotopes in illite-smectite: The importance of crystal size. *Geochimica et Cosmochimica Acta*, *69*(24), 5705–5716. https://doi.org/10.1016/j.gca.2005.08.005

Yen, A. S., Ming, D. W., Vaniman, D. T., Gellert, R., Blake, D. F., Morris, R. V., et al. (2017). Multiple stages of aqueous alteration along fractures in mudstone and sandstone strata in Gale Crater, Mars. *Earth and Planetary Science Letters*, *471*, 186–198. https://doi.org/10.1016/j.epsl.2017.04.033